Rodinia to Gondwana evolution record, South Sinai, Egypt: Geological and geochronological constraints

Mohamed Abu Anbar [a], Tamer S. Abu-Alam [b,c], Mohamed F. Ghoneim [a], YunPeng Dong [d], Xian-Hua Li [e,f], Dina H. Ramadan [a,*], Ahmed E. Masoud [a,g]

[a] Geology Department, Faculty of Science, Tanta University, Tanta, Egypt
[b] Arctic Sustainability Lab, Department of Arctic and Marine Biology, Faculty of Biosciences, Fisheries and Economics, UiT The Arctic University of Norway, 9037 Tromsø, Norway
[c] OSEAN-Outermost Regions Sustainable Ecosystem for Entrepreneurship and Innovation, University of Madeira Colégio dos Jesuítas, 9000-039 Funchal, Madeira Island, Portugal
[d] State Key Laboratory of Continental Dynamics, Department of Geology, Northwest University, Xi'an, China
[e] State Key Laboratory of Lithospheric Evolution, Institute of Geology and Geophysics, Chinese Academy of Sciences, Beijing, China
[f] College of Earth and Planetary Sciences, University of Chinese Academy of Sciences, Beijing, China
[g] Nanjing Hongchuang Geological Exploration Technology Service Co., Ltd., China

A B S T R A C T

The geological history of Sinai is complicated and differs from the other parts of the Arabian Nubian Shield. Some rocks in Sinai have a signature from the Grenvillian crust, as evidenced in Wadi Seih area. The ultimate objective of this research is to clarify the progression of episodic island arc accretion events from the amalgamation of Rodinia to the assembly of Gondwana supercontinent.Geochemical, mineralogical, U-Pb zircon geochronological, and thermobarometric studies are considered to constrain the nature and tectonic evolution of Wadi Seih gneisses. The protoliths of the orthogneisses are tonalite, trondhjemite, granodiorite, and granite, which were derived from metaluminous-calc-alkaline magma and formed during island-arc accretion. The paragneisses originated from immature Fe-sand and arkose that were deposited in active continental margin and back-arc basin. The orthogneisses and orthopyroxene-free paragneisses were metamorphosed under amphibolite to low granulite-facies conditions with temperatures from 530 to 775 °C at pressures of 3–7 kb, while the orthopyroxene-bearing paragneisses were metamorphosed under granulite-facies at a temperature of 870 °C and pressures of 5–7 kb. Zircon U-Pb geochronological data of the orthogneisses yields three distinct ages (i.e., the oldest ages are 994 ± 6 Ma and 976.6 ± 6.2 Ma, the second age is 740 ± 6.4 Ma, and the third age is 619.4 ± 4.2). Similar ages are obtained from detrital zircons in paragneisses: 1039 ± 57 Ma, 643 ± 49 Ma, 628 ± 3.7 Ma, and 627 ± 6.6 Ma. These new U-Pb data delineate three episodic Mesoproterozoic to Neoproterozoic island arc events at 1050–900 Ma, 850–700 Ma, and 650–580 Ma. The oldest 1050–900 Ma arcs potentially formed during the Rodinia supercontinent-arc collision, while the 850–700 Ma arcs may have formed during the closure of the Mozambique Ocean. The youngest 650–580 Ma arcs could reflect the Gondwana assembly. The age of metamorphism in this study is constrained by the low Th/U ratio of a zircon grain at 633 ± 10 Ma, which is consistent with other previous studies in other areas in Sinai.

1. Introduction

There is a complex sequence of events involved in the formation of a supercontinent, beginning with the rifting of an old supercontinent, forming a new oceanic crust, then starting subduction and forming volcanic arcs, subsequently colliding among these arcs, and finally experiencing continental-continental collisions (Nance et al., 2014; Wilson et al., 2019; Hassan et al., 2020). As a result of all these processes, different basin types are formed in different tectonic settings (Bentor, 1985; Middleton, 1989; Stoeser and Camp, 1985; Brooijmans et al., 2003; Moghazi, 2003; Jarrar et al., 2003; Eliwa et al., 2008; Be'eri-Shlevin et al., 2011; Johnson et al., 2011; Allen et al., 2015; Daly et al.,

* Corresponding author.
E-mail address: dhamdy58@yahoo.com (D.H. Ramadan).

2018). The resulting basins received varied detrital sedimentary rocks showing the fingerprint of their original tectonic environment. The youngest ages of detrital zircon derived from these sediments constrain the age of the deposition, while the magmatic rocks and ultimate deformation and metamorphism recorded in these basins indicate the chemical, thermal, and elastic structure of the crust (Cawood et al., 2001; Dasgupta, 2020). Therefore, these basins represent the key to understanding the different tectonic processes.

The Arabian-Nubian Shield (ANS) is considered a clear example of continental crust (Johnson et al., 2011) that recorded tectonic events extending from the assembly of Rodinia (Li et al., 2008) to the assembly of the Gondwana supercontinent (Johnson and Woldehaimanot, 2003; Eyal et al., 2014; Yeshanew, 2017; Khudeir et al., 2021). Geochrono-logical studies of the ANS rocks indicate that evidence of Gondwana is more obvious in the Eastern Desert and Saudi Arabia (Loizenbauer et al., 2001; Andresen et al., 2009; Li égeois and Stern, 2010; Zoheir et al., 2021). Meanwhile, the Sinai Peninsula shows an older geochronological signature, which may indicate preservation of an older history (assem-bly of Rodinia), and a younger geochronological signature related to the amalgamation of the Gondwana supercontinent (Abu Anbar et al., 2004; Abu Anbar et al., 2009; Bea et al., 2009; Abu El-Enen and Whitehouse, 2013; Hassan et al., 2014; Eyal et al., 2014; Hassan et al., 2020).

Studying Precambrian Sinai rocks in conjunction with the surrounding metamorphosed arc plutonic rocks is of great value to test concepts about continental growth and the formation of supercontinents. In this contribution, paragneisses and orthogneisses from Wadi Seih area, southern Sinai, are studied petrographically and geochronologically to clarify the progression of episodic island arc accretion events from the amalgamation of Rodinia to the assembly of Gondwana supercontinent to clarify the different successive island arc stages from the assembly of Rodinia to the assembly of Gondwana supercontinent (Fig. 1). The presented data represent an assumption of a model explaining the Mesoproterozoic-Neoproterozoic tectonic evolution of southern Sinai, Egypt.

2. Geological setting and field aspects

The Arabian-Nubian Shield is composed of juvenile Neoproterozoic rocks (Hargrove et al., 2006; Liégeois and Stern, 2010; Robinson et al., 2014). The shield represents gradual accumulation of arc terranes (Patchett and Chase, 2002; Johnson and Woldehaimanot, 2003; Andresen et al., 2009; Abu-Alam et al., 2014). It is composed mainly of low-grade metavolcanic and metasedimentary rocks (Stern, 2008; Hargrove et al., 2006; Stern and Johnson, 2010). The shield is remarkably rich in dismembered ophiolitic rocks (particularly in the Eastern Desert),

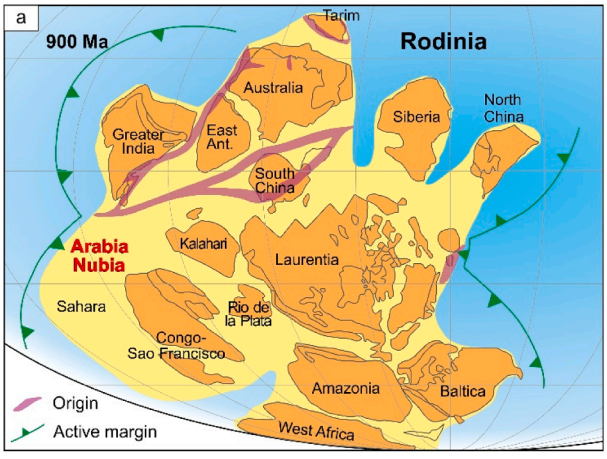

Fig. 1a. Distribution of the Arabian Nubian shield during the Rodinia supercontinent (Li et al., 2008).

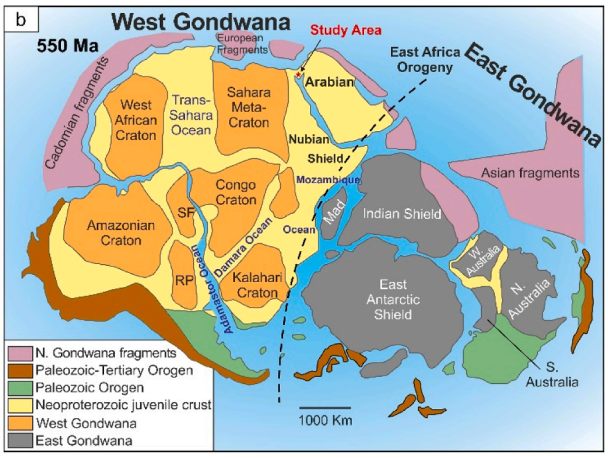

Fig. 1b. Map of Gondwana showing the general arrangement of cratons, shields and oceans at the end of the Neoproterozoic (Gray et al., 2008).

with ages ranging from ca. 890 to 690 Ma (Johnson et al., 2004; Stern et al., 2004). Metamorphic complexes of upper amphibolite facies were exhumed as tectonic windows formed either in extensional (Fritz et al., 1996) or transpressional settings (Abu-Alam and Stüwe, 2009; Meyer et al., 2014). Intermontane basins were formed in association with the exhumation of the metamorphic complexes (e.g., Meyer et al., 2014; Fritz et al., 2002). Granitic magma intruded the shield at various stages of tectonic evolution as syn- and post-tectonic intrusions (Azer et al., 2010; Eyal et al., 2010; Ghoneim et al., 2015a,b).

The Sinai Peninsula occupies the extreme northern part of the ANS. In the southern Sinai Peninsula, the Precambrian basement is built up of four metamorphic complexes (Fig. 2) (namely, Zaghra, Kid, Feiran-Solaf, and Taba) that are separated by voluminous unmetamorphosed granitoid rocks and several Ediacaran volcano-metasedimentary sequences (Eyal et al., 2010; Be'eri-Shlevin et al., 2011). The metamorphic complexes consist of ortho- and paragneisses and schists metamorphosed under conditions of greenschist to amphibolite facies (El-Shafei and Kusky, 2003; Abu El-Enen et al., 2004; Abu Anbar et al., 2004; Eliwa et al., 2008; Abu-Alam and Stüwe, 2009).

The study area (i.e., Seih area; Fig. 2) represents the northwestern extension of the Feiran-Solaf complex. It is composed of orthogneisses, paragneisses, migmatites, syn- and post-tectonic intrusions, and volcanics. These rock units cover the time span from 1000 Ma (Rodinia collision) to 580 Ma (Gondwana assembly).

2.1. *Paragneisses*

They are exposed only in Wadi Tayeba and partly in Wadi Umm Agraf (Fig. 2). They are buff and gray-colored, medium to coarse-grained (1–5 mm), and strongly foliated. They preserve sedimentary layering (S_0, Fig. 3a). Two essential varieties of paragneisses are observed, namely orthopyroxene-free paragneisses and orthopyroxene-bearing paragneisses.

2.1.1. *The orthopyroxene-free paragneisses*

They are composed of quartz, feldspar, garnet, biotite, muscovite, and cordierite. The alternation between gray-colored paragneisses (composed mainly of quartz, feldspar, garnet, biotite, and muscovite) and buff-colored paragneisses (composed mainly of quartz, feldspar, and garnet) defines the original sedimentary layering (S_0). Amphibolitic bands (*para*-amphibolite) and leucosomes are observed in parallel to the S_0.

Four sets of planar structures are observed in these rocks. The first set (S_0) dips 25° toward S50°E. The second set (S_1) forms sub-horizontal foliation planes (i.e., dips 20°-30° toward S50°E), which are defined

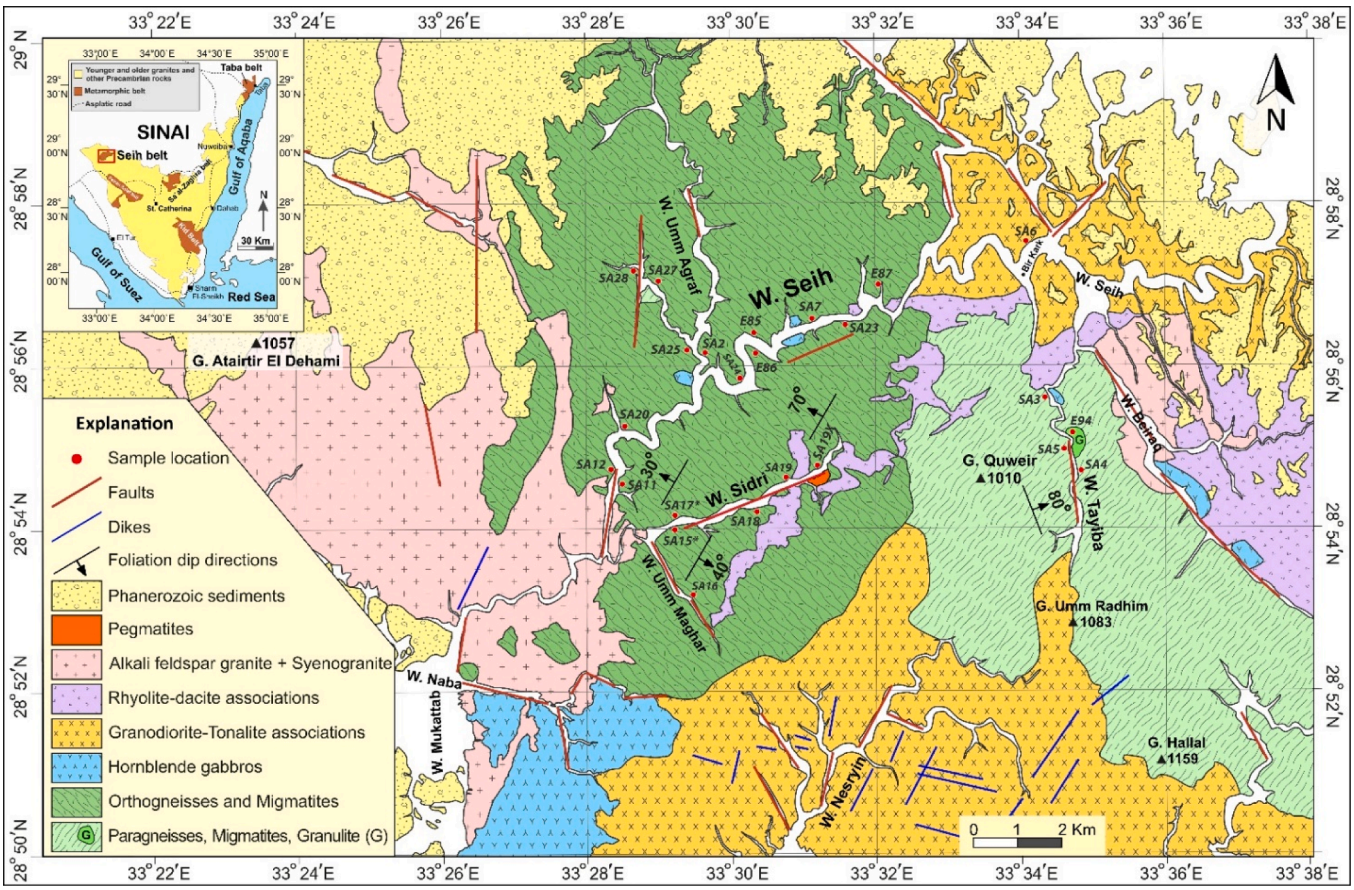

Fig. 2. Geological map of the district around Wadi Seih, Southwest Sinai, Egypt.

by leucosomes and quartz veins parallel to the S_0 (Fig. 3a). Vertical foliation (i.e., S_2) dipping > 50° toward S40°E is observed at Wadi Umm Agraf (Fig. 2b). The S_2 foliation planes are folded to form open-folds with axial planes (S_3) dipping ca. 35° toward N30°E (Fig. 3b).

2.1.2. *Orthopyroxene-bearing paragneisses (granulite)*

They crop out as an elongated (0.8 km in length, 0.2 km in width) outcrop at the central part of Wadi Tayeba (Fig. 2) and are trending N-S. These rocks are medium to coarse-grained (1–4 mm), pinkish to dark gray rocks. S_0 and S_1 planar structures are observed as vertical foliation plans that dip 83° toward the east (Fig. 3c). Orthopyroxene-bearing paragneisses are interbedded with amphibolite bands (*para*-amphibolite), quartz veins, and leucosomes (i.e., defining the S_1, Fig. 3d). S_2 and S_3 are not observed.

The contacts between orthopyroxene-bearing paragneisses and the orthopyroxene-free paragneisses are invisible (i.e., lie in Wadis). The contact between the orthopyroxene-bearing paragneisses and the granodiorite-tonalite associations is a structural contact, whereas the orthopyroxene-bearing paragneisses are thrust over the granodiorite-tonalite associations along the NS plan (Fig. 3c). Sigma bodies and boudinage structures at the thrust plane indicate movement top to the east.

2.2. *Orthogneisses*

They are well exposed at Wadi Seih, Wadi Sidri, Wadi Umm Maghar, and Wadi Umm Agraf, and their area occupies about 180 km^2 (Fig. 2). They are gray or pink in color, medium- to coarse-grained (2–5 mm) with moderate to high relief, and have a granitic composition. They are composed mainly of plagioclase, quartz, hornblende, biotite, and a minor amount of K-feldspar. In some places, they show structural features such as boudinage structure. The outcrops are dissected by major faults trending NE-SW and are crosscut by a number of NE-SW-trending dykes of varying composition. The orthogneisses at Wadi Seih are intruded by Ataitir El Dehami granites. Hornblende gabbros intrude into the orthogneisses and send offshoots and apophyses into them. These gneisses are the extention of the orthogneisses of Feiran Solaf Metamorphic Complex (Abu Anbar and Abd El-Wahed, 2004; Abu-Alam and Stüwe, 2009). Amphibolite (*ortho*-amphibolite) occurs as enclaves or bands alternating with orthogneisses. In the present study, the *ortho*-amphibolite was most probably derived from basic dykes invading the granitic rocks before metamorphism as what was observed in Feiran-Solaf Metamorphic complex (El-Tokhi, 1992).

The orthogneisses at Wadi Um Maghar (in the southern part of the study area, Fig. 2) are characterized by S_1 foliation plans dipping 40° toward S60°E. In contrast, the foliation at Wadi Sidri (in the southern part of the study area) is inclined toward N40°W with a dip amount of about 30°, indicating the occurrence of an antiform fold with a fold axis (S_2) parallel to Wadi Sidri (Fig. 2). On the southern side of Wadi Seih, the foliation (S_1) is inclined toward S35°E with a dip amount of 40°, indicating the existence of a synform with an axial plan (S_2) trending ENE-WSW. Sigma bodies and boudinage structures indicate pure shear and flatting tectonics associated with S_1 foliation (Fig. 3e).

At Wadi Sidri, orthogneisses are frequently crosscut by coarse-grained pegmatitic veins, which show pinch, swell, and boudinage structures in some places. The pegmatitic veins are affected by an open folding with a fold axis (*S3*) trending N30°W (Fig. 3f).

2.3. *Migmatites*

Migmatites occur in both paragneisses and orthogneisses. Migmatites in paragneisses occur along the contacts between paragneisses and

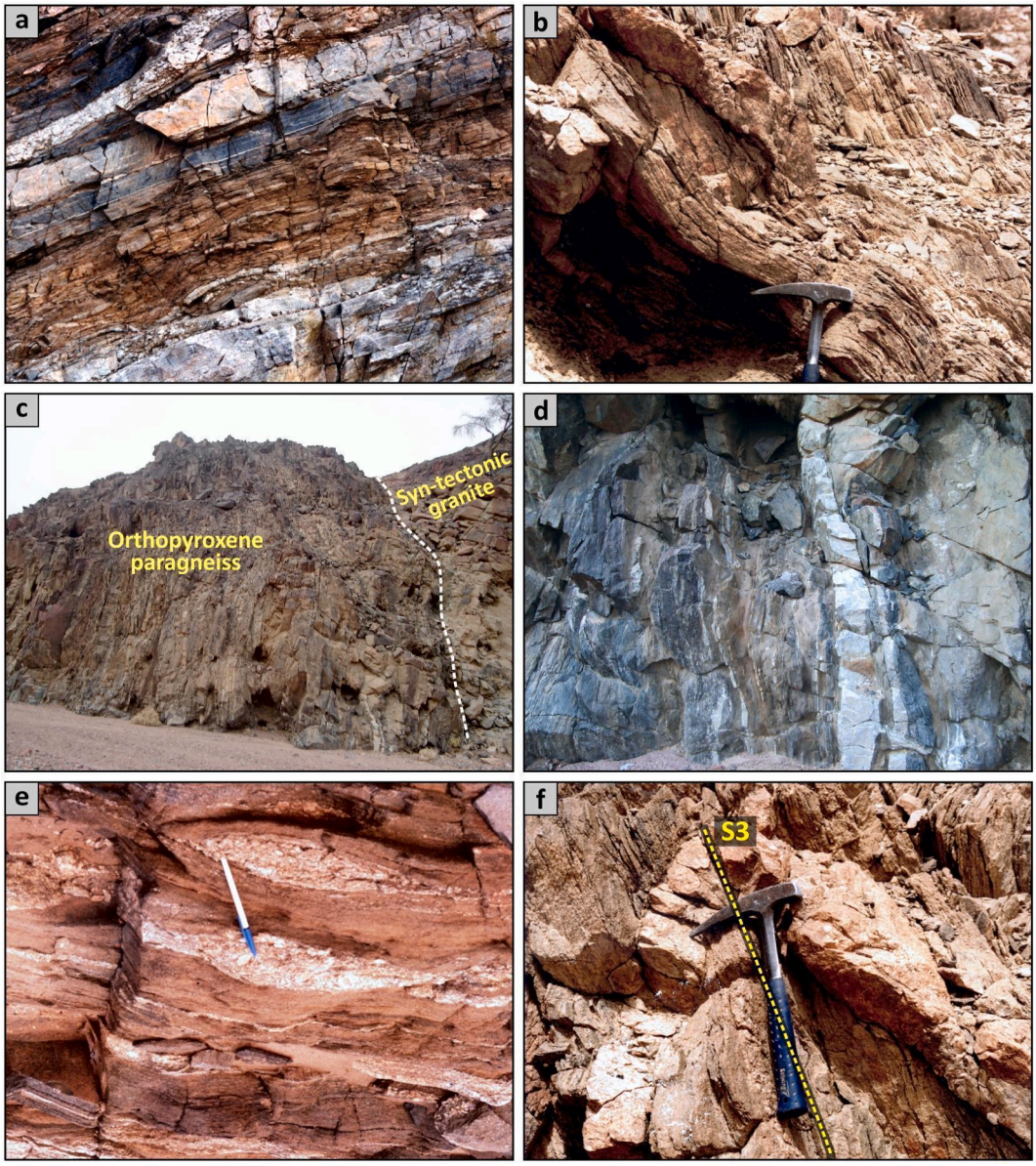

Fig. 3. Field photographs (a) Orthopyroxene free-paragneisses preserve sedimentary layering (S_0), leucosomes and quartz veins (S_1) parallel to the S_0, (b) Vertical foliation (S_2) at Wadi Umm Agraf that folded to form open-folds with axial planes (S_3), (c) Vertical foliation plans (S_0, S_1) of orthopyroxene bearing-paragneisses, that are thrust over the *syn*-tectonic granites along the NS plan (d) Orthopyroxene bearing-paragneisses are interbedded with amphibolite bands, quartz veins, and leucosomes, (e) Sigma bodies and boudinage structures in orthogneisses, (d) The pegmatitic veins in orthogneisses are affected by an open folding with a fold axis (S_3).

granodiorite-tonalite associations. They are distinguished from the paragneisses by typical leucosomes, such as light color, medium- to coarse-grained (2–6 mm), and absence of gneissosity. Stromatic migmatites (Fig. 4a) are the most common type. There are two types of migmatites observed in the orthogneisses; migmatites with a folding structure that show an irregular fold pattern and migmatites with a ptygmatic folding structure.

2.4. Amphibolites

The amphibolites are classified based on both field observations and the geochemical data that interpreted later into ortho and *para*-amphibolites.These rocks are fine to medium-grained massive (*ortho*-amphibolite) to foliated (*para*-amphibolite) greyish green to black in color.The foliated variety varies from slightly foliated to well-developed schistose types. The amphibolites occur as enclaves, bands and linear bodies of variable thickness in para and orthogneisses as unmapped unit (Fig. 3d and 4b). They are composed mainly of hornblende, plagioclase feldspar, opaque, and minor amounts of biotite and quartz.

2.5. Hornblende gabbros

They are exposed at Wadi Naba in the southwestern part of the study area. They occupy an area of about 18 km^2 as well as small masses at the intersection between Wadi Seih and Wadi Umm Agraf, Wadi Tayeba, Wadi Seih, and Wadi Baraq. The hornblende gabbros are coarse-grained (up to 5 mm), dense, and grayish-colored. The gabbroic intrusion exhibits sharp intrusive contacts with the gneisses and sends offshoots and apophyses into them. The gabbroic intrusion contains enclaves from the ortho- and paragneisses in different forms, such as irregular enclaves or sheets from gneisses (Fig. 4c).

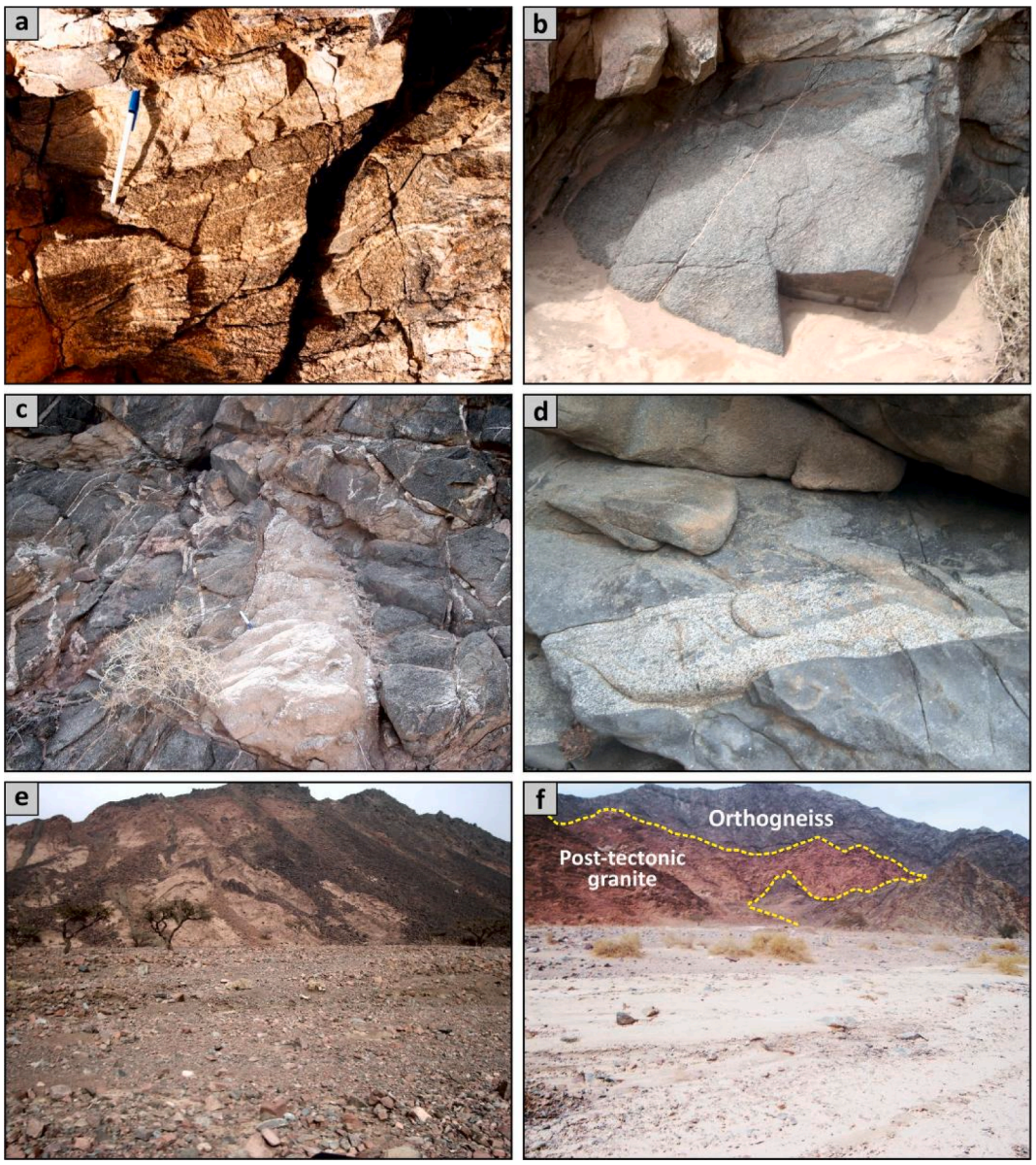

Fig. 4. Field photographs (a) Stromatic migmatites of paragneisses, (b) Amphibolite as enclaves inside orthogneisses, (c) Enclaves of gneisses inside hornblende gabbros, (d) Granodiorite-Tonalite associations intruded as sheet into hornblende gabbro, (e) Volcanics cutting by basic dykes trending NE-SW, (f) The alkali-feldspar granite and syenogranite intrude into the gneisses with sharp intrusion contact.

2.6. Granodiorite-tonalite associations

Granodiorite-tonalite associations (90 km^2) are exposed at the extreme northeastern part of Wadi Seih and the southern part of the mapped area at Gabal Umm Radhim and Gabal Hallal (Fig. 2). They are whitish-gray to dark-gray in color and coarse- to medium-grained (1–5 mm) with a massive appearance. Granodiorite-tonalite associations intrude into the hornblende gabbros (Fig. 4d). They contain xenoliths and mafic fragments.

2.7. Volcanics (rhyolite-dacite associations)

In the studied area, volcanic rocks are exposed at various locations, as shown in Fig. 2. They are hard, massive, gray-rose, and gray-brown to buff in color. They extruded onto the paragneisses and the late to *syn*-tectonic granites. At Wadi Baraq, the volcanics extruded onto the hornblende gabbros and, ultimately, were intruded by alkali feldspar granite and by NE-SW trending mafic dykes (Fig. 4e).

2.8. Alkali-Feldspar granite and syenogranite

They (70 km^2) are located at the NW part of the mapped area (i.e., G. Ataitir El Dehami). The outcrops have high to moderate relief with medium- to coarse-grained rocks (2–5 mm). They intruded into the gneisses with sharp intrusion contact (Fig. 4f). The plutons send apophyses into the country rocks. The granites of G. Ataitir El Dehami are cut by joints, mafic and felsic dykes trending NE-SW.

3. Petrography

3.1. Orthopyroxene-free paragneisses (OPX-FG)

Orthopyroxene-free paragneisses consist of quartz, plagioclase, K-feldspar, garnet, and biotite, in addition to a small amounts of muscovite, cordierite as well as spinel, apatite, zircon, and magnetite. Chlorite and sericite are secondary minerals. These rocks are characterized by a porphyroblastic texture. Garnet grains occur in two forms, the first form

occurs as large deformed garnet porphyroblasts 0.4 to 0.8 mm that are replaced by muscovite, biotite, and cordierite (Fig. 5a), and commonly include inclusions of quartz, plagioclase, and magnetite. The second form of the garnet occurs as euhedral crystals 0.1 to 0.3 mm within a groundmass of quartz, plagioclase, and biotite (Fig. 5b).

Cordierite occurs as porphyroblasts (0.2–0.4 mm) or as a granular aggregate rimming and/or replacing the older form of garnet porphyroblasts. Muscovite occurs as irregular patches (0.15–0.5 mm) between the minerals that grow in equilibrium with the second form of garnet and also occurs as fine crystals in the groundmass. Biotite mostly occurs as flakes in the groundmass. On the other hand, biotite occurs around the rims of garnet porphyroblasts (second phase) or as tiny flakes that grow along the cracks within the porphyroblasts. Some of the biotite and muscovite are overprinted by retrograde chlorite.

Quartz usually occurs as xenoblastic grains 0.1 to 0.4 mm showing irregular outlines or aggregates of small rounded grains. Plagioclase (An_{15-30}) occurs as subhedral to euhedral crystals, ranging in size from 0.2 to 0.6 mm. The twinning is generally albite in form. K-feldspars occur as xenoblast crystals 0.1 to 0.2 mm with irregular to partly regular boundaries. They are usually altered to sericite and show perthitic exsolution.

Chlorite is a secondary alteration product of biotite and muscovite. Sericite is the alteration product of k-feldspar. Magnetite occurs as irregular grains or fine particles with reddish-brown color scattered over the other minerals or as inclusions inside the garnet. Apatite occurs as colorless, elongated crystals that scatter over the different minerals.

3.2. *Orthopyroxene-bearing paragneisses (OPX-BG)*

The mineral assemblages of these rocks include orthopyroxene, clinopyroxene, plagioclase, k-feldspar, garnet, and quartz, as well as minor amounts of hornblende. Zircon, apatite, magnetite, and ilmenite are

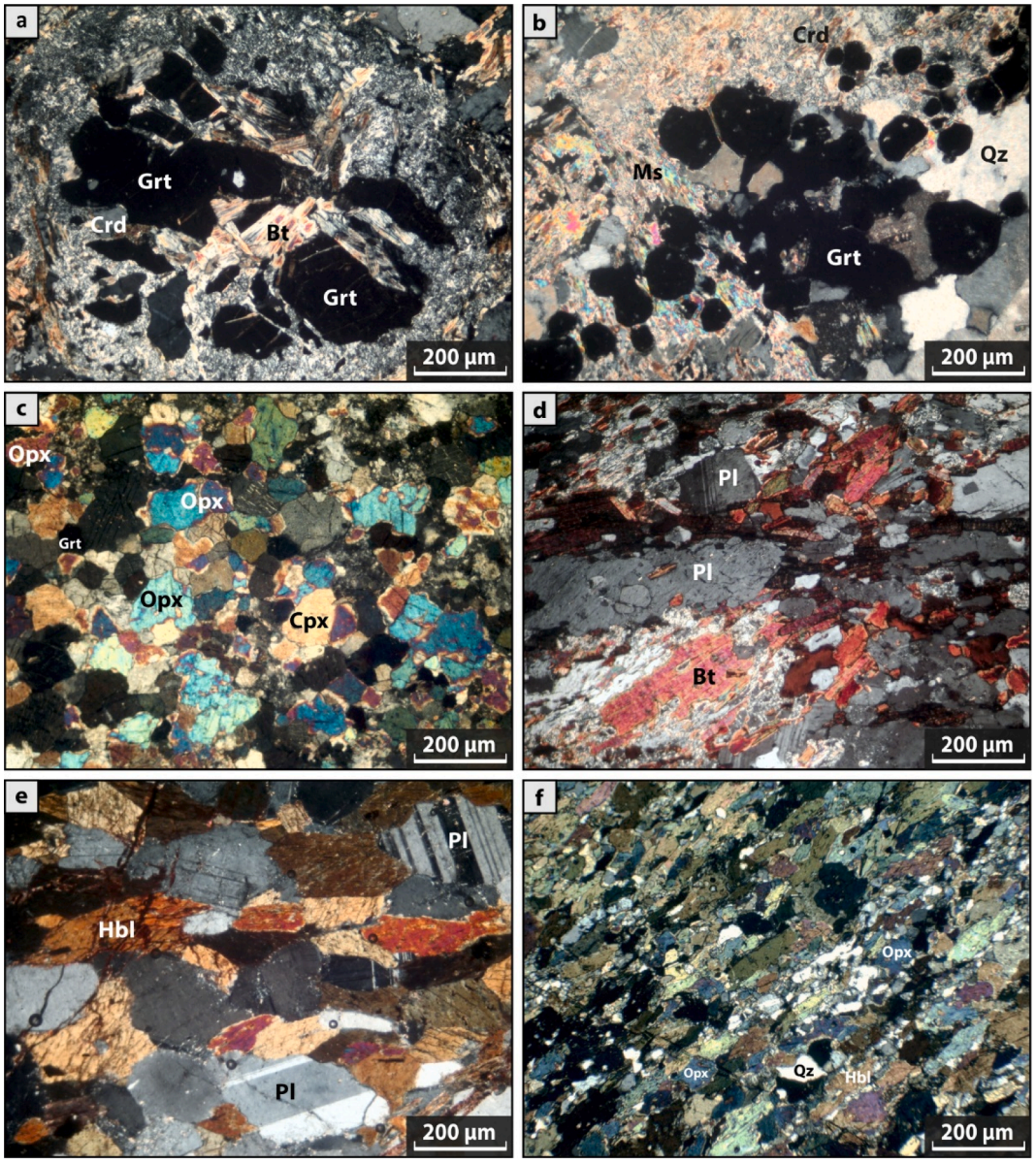

Fig. 5. Cross-polarized (XPL) photomicrographs of the main rock types. (a) Large deformed garnet porphyroblasts that are overprinted by muscovite, biotite and cordierite, (b) Garnet occurs as euhedral crystals in a groundmass of quartz, plagioclase, and biotite, (c) Granoblastic and gneissose textures in orthopyroxene bearing-paragneisses, (d) Biotite gneisses showing alteration of biotite to muscovite, (e) Hornblende gneisses showing plagioclase with high ca content, (f) Para-amphibolite with some relics of pyroxene. Symbols inside the photo: Grt, Garnet; Crd, Cordierite; Qz, Quartz; Px, Pyroxene; Pl, Plagioclase; Hbl, Hornblende; Ms, Muscovite; Bt, Biotite; Opx, Orthopyroxene; Cpx, Clinopyroxene.

common accessory minerals. Secondary minerals are represented by sericite and epidote. They are characterized by granoblastic (Fig. 5c) and gneissose textures.

Orthopyroxene is mainly represented by hypersthene, whereas clinopyroxene is represented by augite and diopside. Hypersthene is yellowish green in color, forms prismatic crystals, and displays strong pleochroic. Hedenbergite is purplish brown, occurring mainly as stubby prismatic crystals with high relief. Diopside is colorless to pale brown with second-order interference color.

Plagioclase (An_{66-92}) forms large subhedral prismatic and tabular grains. It shows lamellar twinning and is sometimes altered to epidote. Garnet is colorless to pale brown, subhedral to euhedral and fills the interstitial space between pyroxene crystals. K-feldspar occurs as perthite and is present in a small amount. Quartz crystals range from subhedral to anhedral and are mostly interstitial between other constituents.

3.3. Orthogneisses

Orthogneisses include three subtypes according to their mafic contents, namely, biotite gneisses (plagioclase + quartz + biotite) (Fig. 5d), hornblende gneisses (plagioclase + quartz + hornblende) (Fig. 5e), and hornblende biotite gneisses (plagioclase + quartz + biotite + hornblende). Minor amounts of k-feldspar are recorded in addition to iron oxides as accessory minerals. Chlorite and sericite are common secondary minerals. They commonly show inequigranular texture with weak foliation.

Plagioclase (An_{27-50}) occurs as anhedral to subhedral elongated crystals up to 0.7 mm in diameter. The crystals show albite and albite-Carlsbad twinning, but untwined crystals are also observed. Quartz occurs as anhedral to subhedral crystals (0.1–0.4 mm) that fill the interstices between plagioclase, hornblende, and biotite crystals. It frequently exhibits undulose extinction. K-feldspar occurs as very small anhedral equant crystals, which lie interstitially between plagioclase, quartz, hornblende, and biotite crystals.

Hornblende occurs in two varieties: brown (hornblende gneisses) and green (hornblende biotite gneisses). Brown hornblende is strongly pleochroic, ranging from yellowish-brown, pale brown, to dark brown, and occurs as anhedral elongated crystals between the plagioclase crystals. Green hornblende has a pleochroism that ranges from green to yellow-green to dark- green and is found as elongated crystals ranging in size from 0.18 to 0.75 mm. Hornblende crystals have retrogressed to chlorite. Biotite occurs as anhedral to subhedral flaky and stumpy crystals ranging in size from 0.2 to 0.4 mm. Chlorite is pale green in color. Sericite occurs as minute shreds after k-feldspar. Magnetite occurs as xenoblastic grains distributed throughout the rock.

3.4. Amphibolites (ortho and para-amphibolite

These rocks are composed mainly of hornblende, actinolite, and plagioclase, with a minor amount of quartz and biotite. Some relics of pyroxene occur in some *para*-amphibolites that are associated with OPX-BG (Fig. 5f). Magnetite and apatite are the common accessory minerals whereas chlorite and epidot are the common secondary minerals. Hornblende occurs as large subidioblastic to xenoblastic grains ranging in size from 2 to 5 mm. Actinolite occurs as colorless prismatic crystals. Plagioclase crystals occur as subidioblastic grains, commonly have albite twinning, and are moderately altered to epidote. Large plagioclase grains contain inclusions of quartz, hornblende, and magnetite. Quartz occurs as equant grains with irregular grain boundaries and sometimes as interstitials between hornblende and plagioclase crystals. Biotite occurs as small flakes (Supplementary Fig. 1a).

3.5. Hornblende gabbros

They are composed mainly of plagioclase and hornblende. Accessory minerals include magnetite and apatite. Sericite occurs as a secondary mineral. These rocks show hypidiomorphic, ophitic, and sub-ophitic textures (Supplementary Fig. 1b).

Plagioclase (An_{35-70}) occurs as twinned subhedral crystals enclosed by hornblende, ranging in size from 0.2 to 0.7 mm. Hornblende occurs either as partly twinned euhedral or subhedral prismatic crystals ranging in size from 0.25 to 0.8 mm and sometimes includes inclusions of quartz and plagioclase. Quartz occupies the interstices between plagioclase and hornblende. Apatite is associated with plagioclase. Iron oxides are represented by anhedral grains of magnetite, which sometimes form clusters or scattered ones.

3.6. Granodiorite

They are characterized by medium to coarse-grained and exhibits equigranular hypidiomorphic texture. They consist mainly of plagioclase (40 to 50% by volume). Quartz represents about 30%, whereas k-feldspar constitutes about 15% of the rock. The mafic minerals are represented by hornblende and biotite. Accessory minerals are apatite, titanite and magnetite. The secondary minerals are sericite and chlorite.

Plagioclase forms euhedral to subhedral elongated crystals, ranging in size from 0.5 to 1.1 mm. It shows normal zoning and albite twinning (Supplementary Fig. 1c). Quartz forms anhedral to subhedral coarse crystals (up to 0.7 mm) and fills the interstices between feldspar crystals. K-feldspars occur as subhedral to anhedral medium-grained crystals, and are represented by orthoclase and perthite crystals. Biotite forms anhedral to subhedral flakes with a brown color. Hornblende occurs as euhedral to subhedral prismatic crystals of green color. Chlorite is the main secondary mineral after biotite.

Sericite occurs as an altered product of K-feldspar. Iron oxides occur either as fine grains along the cleavage planes of biotite and hornblende or as subhedral grains throughout the rock. Apatite occurs as fine prismatic crystals in quartz and feldspar crystals.

3.7. Rhyolite

Rhyolite is composed mainly of phenocrysts of quartz, potash feldspar, and plagioclase set in a microcrystalline groundmass of the same minerals. Chlorite and sericite are the main secondary minerals. Iron oxides, zircon, apatite, and titanite are accessories. The rock shows porphyritic and spherulitic textures (Supplementary Fig. 1d).

3.8. Alkali feldspar granites

They are composed mainly, of k-feldspar (>90%) and quartz, with a minor amount of plagioclase and biotite. Zircon, iron oxides, and apatite are the common accessory minerals, while chlorite and sericite are secondary minerals. They show hypidiomorphic and perthitic textures (Supplementary Fig. 1e).

K-feldspars (microcline and orthoclase) form euhedral to subhedral crystals (up to 1.2 mm in size) with rarely perthitic texture (Supplementary Fig. 1e). Microcline occurs as subhedral crystals with cross-hatched twinning (Supplementary Fig. 1f). Quartz forms anhedral to subhedral crystals up to 0.6 mm, filling the interstices between the feldspar crystals. Plagioclase is commonly albite and forms tabular crystals. Biotite forms small flakes and is partly altered into chlorite. Sericite occurs as an altered product of k-feldspar.

4. Analytic techniques

4.1. Microprobe analyses

Mineral analyses have been performed at the Department of Mineralogy and Petrology, Institute of Geological Sciences, Wroclaw University, Poland, using an electron microprobe (Cambrian Microscan Mg). The analytical conditions were carried out at 15 kv accelerating voltage,

50nA beam current, and 15 s counting time. The chemical formulae are calculated using MinPet software (Richard, 1995) and listed in Tables 1-2 and Supplementary Tables (S1-S8).

4.2. Bulk-rock XRF analyses

Representative rock samples from the paragneisses and orthogneisses were analyzed for major, trace, and rare earth elements by X-ray fluorescence spectrometry (XRF) on pressed powder pellets using an ARL Advant–XP spectrometer, following the full matrix correction method proposed by Lachance and Traill (1966). All analyses were carried out in the laboratories of Ferrara University, Italy. Bulk-rock analysis data are listed in Table 4.

4.3. Zircon U–Pb isotopic analyses

Representative rock samples of paragneisses and orthogneisses from Wadi Seih area were crushed using a disk mill. Zircons were separated from the crushed samples using heavy liquids and conventional magnetic separation. The hand-picked zircons were set in epoxy resin and polished to display the interior of the zircon grains. Transmitted and reflected light microscopes were used to examine zircon grains and imaged them by cathodoluminescence (CL). The Cathodoluminescence (CL) study was carried out at the Institute of Geology and Geophysics, Chinese Academy of Sciences, Beijing (IGG-CAS) using a field emission scanning electron microscope (Nova NanoSEM 450) equipped with GatanMonoCL4 detector.

U–Pb isotopic analyses were performed by secondary ion mass spectrometer (SIMS) using a CAMECA IMS-1280 HR instrument. The operation and data processing techniques follow the guidelines set by Li et al. (2009). An O_2 primary ion beam accelerated at 13 KV with an elliptical spot size of ca. 30 μm × 20 μm was used in the analyses. The zircon standard 91,500 (Wiedenbeck et al., 2004) was used to calibrate the SIMS analyses. Long-term uncertainty of 1.5% (1σ RSD) for $^{206}Pb/^{238}U$ measurements of the standard zircons was propagated to the unknown (e.g., Li et al., 2010), despite the measured $^{206}Pb/^{238}U$ error in a specific session being generally ≤ 1% (1σ RSD). A non-radiogenic ^{204}Pb and modern terrestrial Pb model of Stacey and Kramers (1975) were used for the common Pb lead correction, assuming that the common Pb is largely surface contamination introduced during sample preparation. Calculations use the routines of the Isoplot program (Ludwig, 2007). U–Pb isotopic analyses are listed in Supplementary Tables (S9-S10).

5. Mineral chemistry

Electron microprobe (EMP) analyses of the amphibole minerals and their chemical formulae based on 23 oxygen atoms are listed in Table 1 and Supplementary Table (S1). The analyzed amphiboles of the gneisses and amphibolites are classified according to the classification of Leake et al. (1997) as members of calcic amphiboles (Ca > 1.5). The analyses are plotted on the TSi versus (Mg/Mg + Fe) diagram after Leake, 1978 (Fig. 6a and b), and they reveal that the *para*-amphibolites are magnesio-hornblende with a few actinolite-hornblende and edenite.With respect OPX-BG, the studied amphiboles are ferro-hornblende, magnesio-hornblende, tschermakite hornblende, Fe tschermakite hornblende, and ferro- edenitic hornblende.

The mineral chemistry of orthogneisses and *ortho*-amphibolite indicate that they are edentitic hornblende, ferro-edenitic hornblende, and ferroan pargasite.The studied amphiboles show the chemical signature of a metamorphic amphibole (Fig. 6c).

The results of EMP analyses of biotite minerals and their chemical formulae, which were calculated on the basis of 24 oxygen atoms, are listed in Table 1 and Supplementary Table (S2). The chemical contents (i.e., Al, Fe^{3+}, Ti, Mg, Fe^{2+} and Mn) of the biotite of OPX-FG and orthogneisses reveal that the studied biotites have a siderophyllite, Fe biotite and Fe, Mg-biotite composition; respectively (Fig. 6d and e).

Muscovite chemical composition of OPX-FG and their structural formulae based on 24 oxygen atoms are given in Table 1 and Supplementary Table (S3). Muscovite has high Al_2O_3 and K_2O contents with an average of 35.24 wt% and 11.38 wt%, respectively, and a moderate SiO_2 content with an average of 45.41 wt%. The studied muscovite is classified as primary muscovite (e.g., Miller et al., 1981).

The chemical formulae of the feldspar of paragneisses, amphibolites and orthogneisses were computed on the basis of 8 oxygen atoms and is listed in Table 2 and Supplementary Table (S4).

The plagioclase of OPX-FG has an oligoclase composition (Fig. 6f) while, *para*-amphibolites have a bytownite composition. Their XCa average (Ca/Ca + Na) are 0.207 and 0.866, respectively.The plagioclase of the OPX-BG has a compositional range between labradorite and anorthite, with an XCa ranging from 0.671 to 0.968 (with an average of 0.833). The plagioclase of the orthogneisses has a composition range from oligoclase to andesine with an XCa average 0.297,while *ortho*-amphibolites have andesine to a labradorite composition with an XCa average 0.476.

Chemical analyses and structure formulae of pyroxenes from OPX-BG based on 6 oxygen atoms are listed in Table 2 and Supplementary Table (S5). The analyzed pyroxenes of the studied granulite are classified as Ca-rich pyroxenes and Ca-poor pyroxenes. In the Wo-En-Fs classification diagram of Morimoto (1988). Ca-poor pyroxenes of the studied granulite (orthopyroxene) have a composition between pigeonite and clinoferrosillite, with X_{Fe} ranging from 0.505 to 0.576 (with an average of 0.526). In contrast, Ca-rich pyroxenes (clinopyroxene) have a composition between diopside and hedenbergite, with X_{Fe} ranging from 0.437 to 0.548 (with an average of 0.500) (Supplementary Fig. 2a).

The garnet formulae of the paragneisses were calculated based on 12 oxygen atoms listed in Table 2 and Supplementary Table (S6). The garnet of the OPX-FG is characterized by low CaO, high Al_2O_3, and high FeO. The composition of garnet in the OPX-FG is mainly almandine and varies from 67.6 to 81.3 mol %, with variable amounts of spessartine, pyrope, and grossular. The values of X_{Fe} range from 0.850 to 0.927, with an average of 0.905.

Garnet of OPX-BG exhibits a solid solution between almandine (41 mol %) and grossular (45 mol %) with variable amounts of spessartine, pyrope, and andradite (Supplementary Fig. 2b). The X_{Fe} ranges from 0.939 to 0.943, with an average of 0.941.

The chemical formulae of the studied chlorite were calculated based on 36 oxygen atoms and are listed in Supplementary Table (S7). Chlorite of orthogneisses has high FeO and MgO contents with an average of 27.64 wt% and 13.75 wt%, respectively, and low content of SiO_2 with an average of 26.51 wt%. The studied chlorite is classified as chamosite according to the nomenclature of Hey, 1954.

The chemical composition of cordierite and its structural formulae based on 18 oxygen atoms are given in Supplementary Table (S8). Cordierite has medium SiO_2 with an average of 47.66 wt% and high Al_2O_3, FeO, and MgO content with an average of 31.03 wt%, 12.11 wt%, and 5.18 wt%, respectively.

6. P-T calculations

Different thermobarometers are used to estimate the metamorphic pressure and temperature conditions and to determine the grade of metamorphism that prevails during rock formation.

6.1. Thermobarometry

6.1.1. Average temperature by using THERMOCALC program

The average temperature has been calculated by the THERMOCALC program. The activities of end-members of plagioclase, orthopyroxene, clinopyroxene, amphibole, garnet, ilmenite, cordierite, biotite, and muscovite are calculated using the program AX (http://ccp14.cryst.bbk.

Table 1
Representative amphibole, biotite and muscovite microprobe analyses.

Rock unit	Para-amphibolite		OPX-BG		Orthogneisses		Ortho-amphibolite	Rock unit	Opx-FG		Orthogneisses		Opx-FG		
Mineral	Amphibole								Biotite				Muscovite		
Analyses/Sa.No.	E94T-gaa	E94T-gba	E94G-fxd	E94G-fad	SA22-maa	SA15-naf	SA19X-oab	Analyses/Sa.No	E94E-hbd	SA4C-kba	SA22-mba	SA15-nbc	SA4F-lba	SA4F-lbb	SA4F-lbf
Core/rim	c	c	c	r	c	r	r	Core/rim					c	r	r
SiO2	46.61	45.52	43.51	47.18	43.08	41.91	43.38	SiO2	33.48	31.97	35.75	35.12	45.64	45.35	45.04
TiO2	0.85	0.69	1.34	0.5	1.11	1.26	1.06	TiO2	2.93	1.37	4.02	3.97	0.39	0.44	0.22
Al2O3	8.16	9.82	11.19	8.64	10.47	10.11	12.1	Al2O3	17.49	19.01	14.31	13.86	36.61	35.12	34.01
MnO	0.36	0.39	0.72	0.74	0.48	0.9	0.44	FeO	26.02	24.60	19.96	25.29	1.29	1.33	1.25
FeO	11.8	12.92	13.93	9.98	14.27	16.86	15.92	MnO	0.23	0.11	0.31	0.54	0.02	0.00	0.02
Fe2O3	3	2.21	5.5	7.99	4.52	5.53	2.73	MgO	4.86	6.71	10.66	7.64	0.45	0.41	0.39
MgO	11.98	11.31	8.68	11.04	9.74	7.19	8.82	CaO	0.36	0.01	0.00	0.01	0.28	0.01	0.01
CaO	11.51	11.63	11.3	11.06	11.37	11.11	11.66	Na2O	0.23	0.10	0.18	0.36	0.62	0.67	0.68
Na2O	1.1	1.48	1.21	0.89	1.78	1.48	1.68	K2O	9.22	8.17	10.81	10.16	10.66	11.78	11.46
K2O	0.72	0.91	0.78	0.37	1.34	1.22	1.13	H2O	3.82	3.86	3.90	3.80	4.50	4.47	4.48
H2O	2.01	2.01	2.01	2.06	2	1.95	2.01	Total	98.64	95.91	99.90	100.75	100.46	99.58	97.56
Total	98.1	98.89	100.17	100.5	100.16	99.52	100.93	Formula							
Formula								#Si IV	5.34	5.19	5.51	5.50	6.05	6.11	6.19
T Si	6.978	6.805	6.54	6.946	6.522	6.483	6.486	#Al IV	2.66	2.81	2.49	2.50	1.95	1.89	1.81
T AlIV	1.022	1.195	1.46	1.054	1.478	1.517	1.514	T site	8.00	8.00	8.00	8.00	8.00	8.00	8.00
T subtotal	8	8	8	8	8	8	8	#Al VI	0.63	0.82	0.11	0.05	3.76	3.68	3.69
C Ti	0.096	0.078	0.152	0.055	0.126	0.147	0.119	#Ti VI	0.35	0.17	0.47	0.47	0.04	0.04	0.02
C AlVI	0.418	0.535	0.523	0.445	0.39	0.326	0.619	#Fe + 2	3.47	3.34	2.57	3.31	0.14	0.15	0.14
C Fe3+	0.168	0.082	0.324	0.427	0.171	0.381	0.102	#Mn + 2	0.03	0.02	0.04	0.07	0.00	0.00	0.00
C Mn2+		0.003	0.007			0.044		#Mg	1.16	1.62	2.45	1.78	0.09	0.08	0.08
C Fe2+	1.645	1.782	2.05	1.65	2.115	2.444	2.194	O site	5.63	5.97	5.64	5.69	4.04	3.96	3.94
C Mg	2.674	2.521	1.945	2.423	2.198	1.658	1.966	#Ca	0.06	0.00	0.00	0.00	0.04	0.00	0.00
C subtotal	5.001	5.001	5.001	5	5	5	5	#Na	0.07	0.03	0.05	0.11	0.16	0.17	0.18
B Mn2+	0.046	0.047	0.084	0.092	0.062	0.074	0.056	#K	1.88	1.69	2.13	2.03	1.80	2.02	2.01
B Fe2+	0.002			0.037	0.036		0.002	A site	2.01	1.72	2.18	2.14	2.00	2.20	2.19
B Ca	1.846	1.863	1.82	1.745	1.844	1.841	1.868	#O	20.00	20.00	20.00	20.00	20.00	20.00	20.00
B Na	0.106	0.09	0.096	0.126	0.058	0.084	0.074	#OH	4.00	4.00	4.00	4.00	4.00	4.00	4.00
B subtotal	2	2	2	2	2	1.999	2	Charge	0.00	0.00	0.00	0.00	0.00	0.00	0.00
A Na	0.213	0.339	0.257	0.128	0.464	0.359	0.413	XFe	0.75	0.67	0.51	0.65	0.62	0.65	0.64
A K	0.138	0.174	0.15	0.069	0.259	0.241	0.216	XMg	0.25	0.33	0.49	0.35	0.38	0.35	0.36
A subtotal	0.351	0.513	0.407	0.197	0.723	0.6	0.629								
O	22	22	22	22	22	22	22								
OH	2	2	2	2	2	2	2								
Sum T,C,B,A	15.35	15.51	15.41	15.20	15.72	15.60	15.63								
(Na + Ca)B	1.952	1.953	1.916	1.871	1.902	1.925	1.942								
(Na + K)A	0.351	0.513	0.407	0.197	0.723	0.6	0.629								
XFe	0.38116	0.41413	0.51314	0.41	0.4946	0.59581	0.527630947								

.

Table 2
Representative plagioclase, pyroxene and garnet microprobe analyses.

Rock unit	Opx-FG		Opx.BG		Orthogneisses		Rock unit	Opx.BG			Rock unit	Opx.FG		Opx. BG
Mineral	Plagioclase						Mineral	Orthopyroxene		Clinopyroxene	Mineral		Garnet	
Analyses/ Sa.No	E94E-hpa	SA4C-kpb	E94G-fpa	SA4A-rpd	SA22-mpa	SA15-npd	Analyses/ Sa.No	E94G-xk	E94G-Xc	SA4A-xb	Analyses/ Sa.No	SA4F-lga	SA4C-kga	SA4A-rgc
Core/rim	c	r	c	r	c	r	Core/rim	c	r	r	Core/rim	c	c	r
SiO2	60.54	62.00	51.95	43.18	61.69	61.21	SiO2	52.93	52.22	50.38	SiO2	36.50	37.20	37.57
Al2O3	26.29	23.13	30.46	35.59	21.45	23.95	TiO2	0.16	0.30	0.02	TiO2	0.00	0.00	0.04
Fe2O3	0.06	0.08	0.10	0.14	0.13	0.13	Al2O3	1.25	2.24	0.72	Al2O3	21.10	21.42	22.12
MgO	0.05	0.02	0.05	0.03	0.03	0.02	FeO	25.03	27.84	16.60	FeO	35.19	35.93	20.05
MnO	0.00	0.02	0.00	0.02	0.02	0.00	MnO	1.74	1.81	0.64	MnO	5.13	1.24	3.44
CaO	5.66	5.30	14.01	19.20	5.94	5.80	MgO	13.72	11.81	7.66	MgO	1.57	3.40	0.71
Na2O	7.34	9.07	3.79	0.35	8.48	7.58	CaO	2.12	2.15	23.02	CaO	0.45	1.70	16.71
K2O	1.30	0.32	0.07	0.01	0.51	0.43	Na2O	0.17	0.19	0.10	Na2O	0.07	0.09	0.03
Total	101.24	99.94	100.43	98.52	98.25	99.12	K2O	0.01	0.05	0.00	K2O	0.00	0.00	0.00
Formula							Total	97.13	98.61	99.14	Total	100.01	100.98	100.67
#Si + 4	2.67	2.76	2.35	2.03	2.80	2.74	Formula				Formula			
#Al + 3	1.36	1.21	1.63	1.97	1.15	1.26	#Si IV	2.07	2.04	1.98	#Si + 4	2.98	2.97	2.95
#Fe + 3	0.00	0.00	0.00	0.01	0.00	0.00	#Al IV	0.00	0.00	0.02	#Ti + 4	0.00	0.00	0.00
#Mg + 2	0.00	0.00	0.00	0.00	0.00	0.00	T site	2.07	2.04	2.00	#Al + 3	2.03	2.01	2.05
#Mn + 2	0.00	0.00	0.00	0.00	0.00	0.00	#Al VI	0.06	0.10	0.01	#Fe + 2	2.40	2.40	1.32
#Ca + 2	0.27	0.25	0.68	0.97	0.29	0.28	#Ti	0.00	0.01	0.00	#Mn + 2	0.35	0.08	0.23
#Na + 1	0.63	0.78	0.33	0.03	0.75	0.66	#Fe + 2	0.82	0.91	0.55	#Mg + 2	0.19	0.40	0.08
#K + 1	0.07	0.02	0.00	0.00	0.03	0.02	#Mn + 2	0.06	0.06	0.02	#Ca + 2	0.04	0.15	1.40
#Total	5.00	5.03	5.00	5.00	5.01	4.97	#Mg	0.80	0.69	0.45	#Na + 1	0.01	0.01	0.00
#O-2	8.00	8.00	8.00	8.00	8.00	8.00	#Ca	0.09	0.09	0.97	#K + 1	0.00	0.00	0.00
Na + K + Ca	0.97	1.05	1.02	1.00	1.06	0.96	#Na	0.01	0.01	0.01	#Total	8.01	8.03	8.03
ab	0.65	0.74	0.33	0.03	0.70	0.68	#K	0.00	0.00	0.00	#O-2	12.00	12.00	12.00
or	0.08	0.02	0.00	0.00	0.03	0.03	M1,M2	1.84	1.87	2.01	End members			
an	0.28	0.24	0.67	0.97	0.27	0.29	#O	6.00	6.00	6.00	Almandine	80.36	78.65	41.82
Xca	0.30	0.24	0.67	0.97	0.28	0.30	XFe	0.51	0.57	0.55	Spessartine	11.90	2.82	7.75
											Pyrope	6.41	13.63	2.81
											Grossular	1.315849446	4.75	45.78
											Andradite	0.00512004	0.15	1.83
											Uvarovite	0	0.00	0.00

ac.uk/ccp/web-mirrors/crush/astaff/holland/ax.html). The estimated temperature range for OPX-BG is 737 °C to 855 °C. In contrast, OPX-FG recorded a temperature range of 585 °C to 685 °C. The recorded assemblage insufficient to apply the average pressure calculation.

6.1.2. *Mineral pairs thermometers*

Different calibrations of the garnet biotite Fe-Mg exchange thermometer were applied to the (OPX-FG) (Table 3). The temperature using the chemistry of garnet cores ranges from 590 to 773 °C (according to the calibrations of Bhattacharya et al., 1992; Thompsons, 1976; Holdaway and Lee, 1977). Garnet rims, on the other hand, record a temperature 464 to 689 °C (according to the calibrations of Bhattacharya et al., 1992; Dasgupta et al., 1991; Perchuk and Lavrent'Eva, 1983).

Different calibrations of the garnet-cordierite thermometer (i.e., Thompson, 1976; Holdaway and Lee, 1977; Bhattacharya et al., 1988; Perchuk et al., 1985; Wells, 1979) were applied for the orthopyroxene-free paragneisses. The chemistry of the garnet-cordierite pairs shows an equilibrium temperature range from 591 to 630 °C (Table 3).

The Al^{tot} of the amphibole vs. Ca plagioclase diagram of Plyusnina (1982) (Fig. 7a) shows that the orthogneisses record a temperature range of 530 °C to 650 °C, whereas the metamorphic pressure is in the range of (4–7 kb). According to the calibration of Holland and Blundy (1994) the orthogneisses record a temperature range of 691 °C to 754 °C.

6.1.3. *Single mineral thermometers*

The plots of the analyzed feldspars on the Or-Ab-An ternary composition diagram of Elkins and Grove (1990) (Fig. 7b) indicate that samples of the OPX-BG show a temperature range of (580 °C – 650 °C). The feldspars of OPX-FG and orthogneisses indicate that metamorphism occurred at a temperature range of (550 °C – 650 °C except for few spots at 800 °C).

The formation temperature of the metamorphic amphibole can be estimated by plotting Al^{IV} on the temperature - Al^{IV} standard diagram of Blundy and Holland (1990). The diagram shows that the metamorphic amphibole in the OPX-BG samples was formed at temperatures ranging from 720 °C to 870 °C. In contrast, the formation temperatures of the metamorphic amphibole of the *para*-amphibolite range between (550–750 °C) (Fig. 7c).

The temperature is determined by plotting the values of Ti and Mg/(Mg + Fe) of biotite on Wu and Chen's (2015) diagram. Fig. 7d shows that the studied OPX-FG indicates a temperature range from 600 °C to 760 °C while, the orthogneisses indicate a temperature range of (680–760 °C) at 4–6 kb.

The thermometer of chlorite has been calculated for orthogneisses using the equation of Cathelineau (1988) ($T = 321.98Al^{IV} - 61.92$). Cathelineau's equation gave a temperature range from 293 to 315 °C.

6.2. *Barometry*

The aluminum content of hornblende can be used as a barometer in igneous systems (Hammarstrom and Zen, 1986; Hollister et al., 1987; Johnson and Rutherford, 1989; Schmidt, 1992). However, can be used as approximately in the metamorphic system. The pressure conditions in our study rocks were calculated based on the average of four equations. The calculated approximate pressure is about (5.8 kb) for the OPX-BG, (3.8 kb) for the OPX-FG and (5.6 kb) for orthogneisses. More detailed calculations are listed in Supplementary Table (S11).

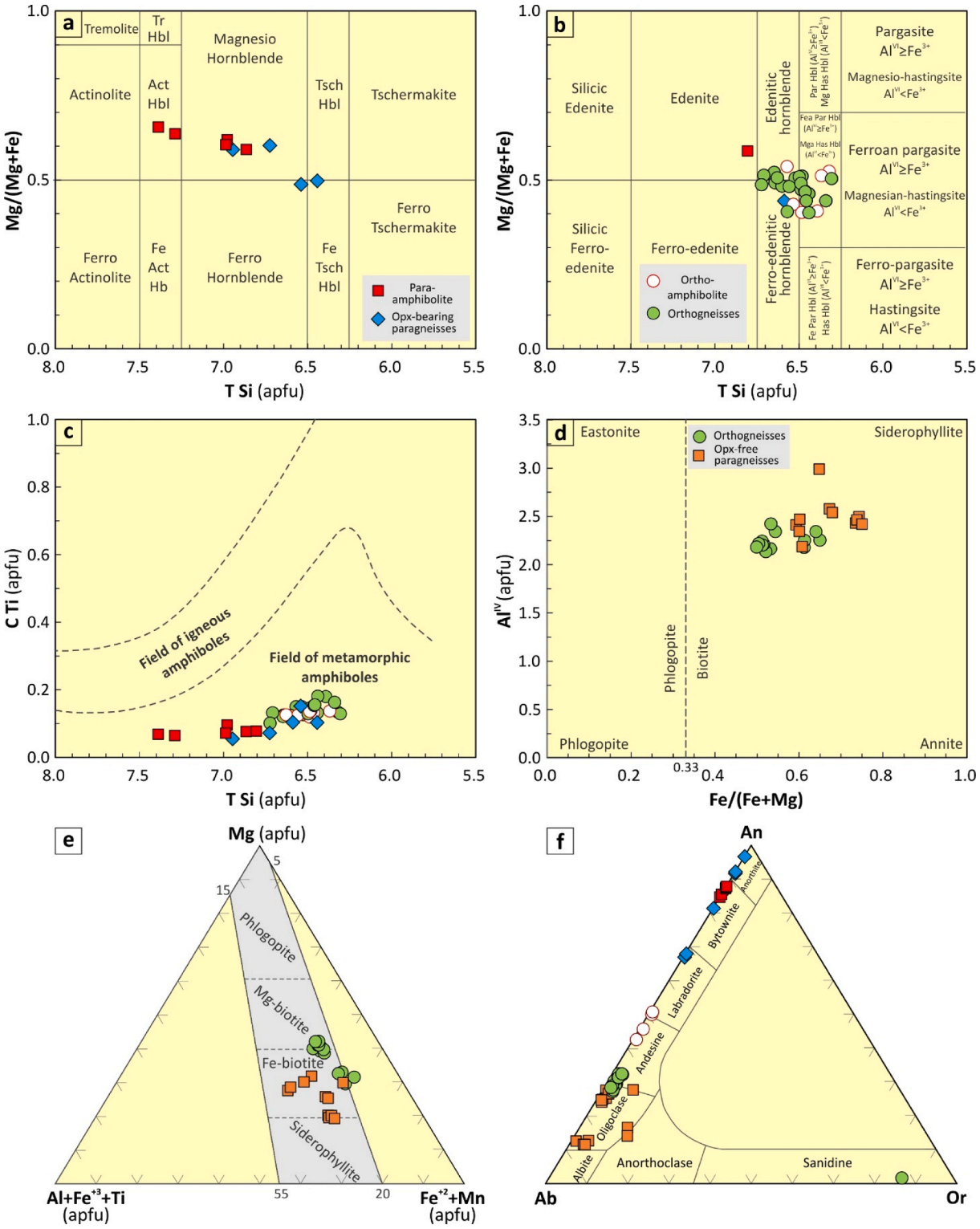

Fig. 6. (a, b) Classification diagram of calcic-amphibole (Leake, 1978), (c) Si vs. Ti diagram for amphiboles of gneisses (Leake, 1965), (d) Al^{IV} vs. Fe/(Fe + Mg) diagram (Deer et al., 1986), (e) Classification diagram of biotite (Foster 1960), (f) Or-Ab-An ternary diagram of plagioclase composition (Deer et al., 1978).

7. Geochemistry

7.1. Orthogneisses

The orthogneisses have a wide range of SiO_2 (56.59–73.48 wt%), Al_2O_3 (13.58–17.08 wt%), Fe_2O_3 (0.83–8.37 wt%), MgO (0.44–5.67 wt %), CaO (1.29–8.23 wt%), Na_2O (3.52–4.55 wt%), Sr (256–955 ppm), Zr (112–231 ppm), Ba (235–665 ppm), and Rb (8–70 ppm). They are rich in ferromagnesian components with (Fe_2O_3 + MgO + TiO_2) > 5.

7.2. Ortho-amphibolite

Ortho-amphibolite shows a low content of SiO_2, enriched in Fe_2O_3, MgO, Ba, Sr, V, Sr, and Cr. SiO_2 ranges from 47.56 to 51.10 wt%, and

.

Table 3
Results of garnet-biotite and garnet-cordierite thermometer.

Thermometer	Garnet-biotite		Thermometer	Garnet-cordierite
Calibrations/ core -rim	Core	Rim	Calibrations	Temperature
Bhattacharya et al., 1992	590–743 °C	571–682 °C	Thompson, 1976	600–630 °C
Dasgupta et al., 1991	562–710 °C	464–664 °C	Holdaway and Lee, 1977	591–617 °C
Perchuk and Lavrent'Eva, 1983	619–713 °C	567–689 °C	Bhattacharya et al., 1988	597–626 °C
Thompsons, 1976	630–773 °C	556–734 °C	Perchuk et al., 1985	592–621 °C
Holdaway and Lee, 1977	623–746 °C	558–713 °C	Wells, 1979	605–615 °C

Na_2O ranges from 2.36 to 4.21 wt%. Al_2O_3 ranges from 11.96 to 18.32 wt%, MgO ranges from 5.77 to 7.39 wt%, and Fe_2O_3 ranges from 10.93 to 18.23 wt%. Ba content is relatively high and ranges from 185 to 404 ppm. Sr ranges from 253 to 376 ppm. Nb content is low and ranges from 1 to 7 ppm. The high content of Ba and Sr may be attributed to the high anorthite content due to metamorphism.

7.3. *Paragneisses and para-amphibolites*

Bulk rock analyses of paragneisses show relatively wide compositional ranges, e.g., SiO_2 (62.56–75.59 wt%), Al_2O_3 (12.52–16.93 wt%), Fe_2O_3 (0.61–6.2 wt%), MgO (0.10–4.06 wt%), CaO (0.6–13.76 wt%), Na_2O (1.48–5.25 wt%), Sr (157–574 ppm), Zr (5–213 ppm), Ba (112–625 ppm), and Rb (4–51 ppm). This variability is attributed to the primary chemical heterogeneity of the protolith. The high SiO_2 and CaO + Na_2O values are due to the high quartz and albite content of their parent protolith. Meanwhile, the compositional ranges of the *para*-amphibolites (Table 4) are narrower such as SiO_2 (49.96–50.06 wt%), Al_2O_3 (11.4–13.67 wt%), Fe_2O_3 (11.51–12.75 wt%), Sr (326–439 ppm), Zr (74–85 ppm),

8. U–Pb zircon geochronology

In order to constrain the age of the protoliths, deposition, and metamorphism of the gneisses in Wadi Seih area,147 spots from eight samples (3 paragneisses and 5 orthogneisses) were selected for U–Pb zircon dating. U–Pb analyses on zircons from the eight samples and their corresponding ages are presented in Supplementary Tables (S9-S10).

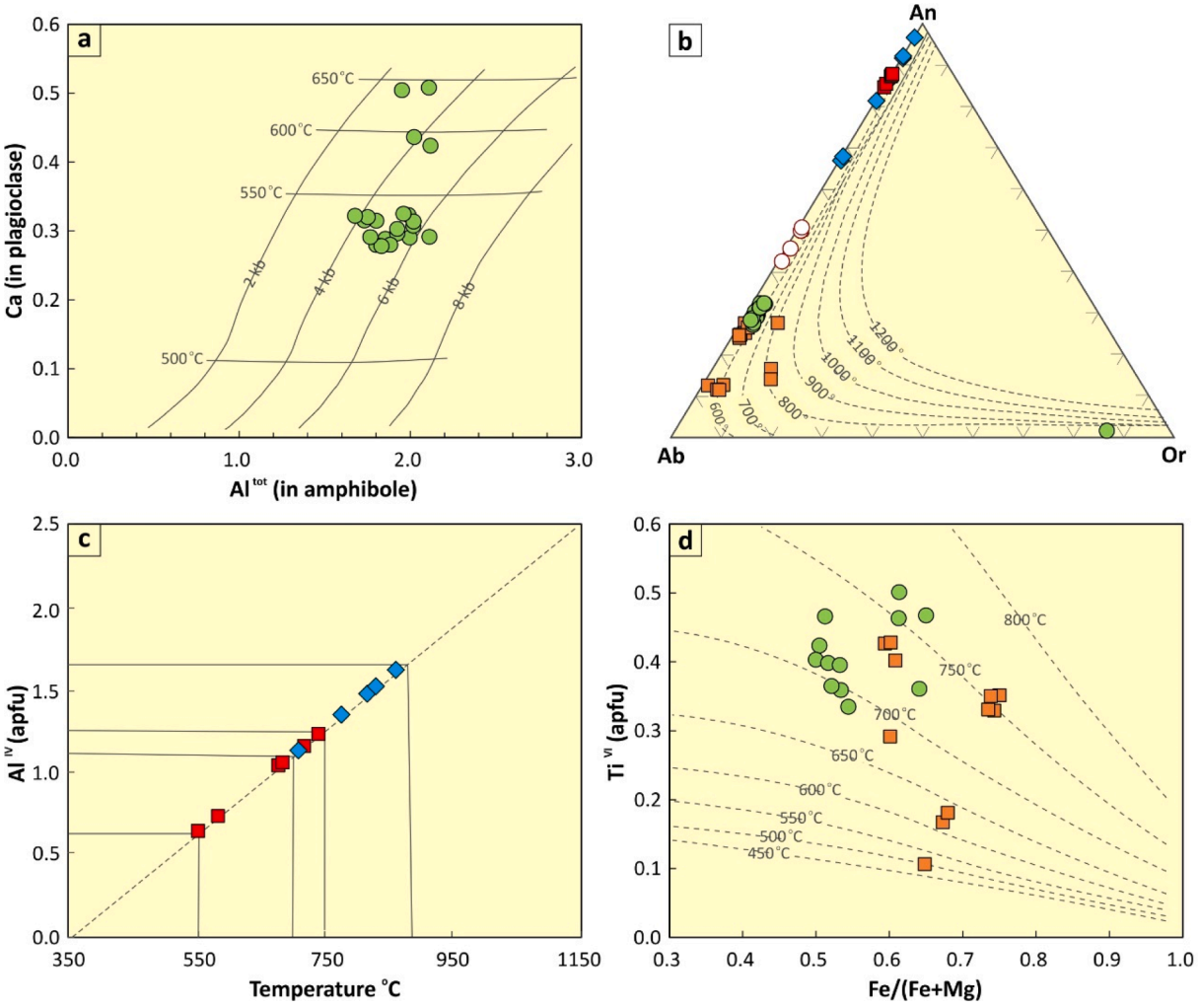

Fig. 7. (a) Al^{tot} of amphiboles vs. Ca of plagioclase coexisting pairs (Plyusnina, 1982), (b) Ternary composition diagram for feldspar with the solvus isotherms (Elkins and Grove, 1990), (c) Temperature–Al^{IV} diagram for amphiboles (Blundy and Holland, 1990), (d) Ti in biotite thermometer, (Wu and Chen, 2015). Symbols as in Fig. 6.

.

Table 4
Chemical analyses of gneisses and amphibolites.

Rock unit	Orthogneisses					Ortho-amphibolite				Paragneisses				Para-amphibolite	
Analyses/Sa. No	E85	E86	SA15a	SA22	SA19	E81	SA8b	SA19x	SA21	E94H	SA4F	SA28	SA4A'	E94T	E94H'
SiO2	56.59	57.90	73.48	60.45	71.43	47.56	50.69	48.64	51.10	75.59	73.83	63.77	62.56	49.96	50.06
TiO2	0.77	1.04	0.33	0.69	0.17	2.18	1.28	1.05	1.33	0.09	0.08	0.82	0.61	1.06	0.99
Al2O3	14.39	16.15	13.58	17.08	15.77	11.96	16.50	18.32	14.51	13.82	16.93	12.52	12.89	11.40	13.67
Fe2O3	8.37	7.61	2.14	5.08	0.83	18.23	12.03	10.93	11.55	0.63	0.61	6.20	4.05	11.51	12.75
MnO	0.29	0.12	0.06	0.08	0.02	0.23	0.30	0.19	0.22	0.05	0.05	0.16	0.15	0.23	0.37
MgO	5.67	4.74	1.05	4.15	0.44	7.19	5.78	5.77	7.39	0.44	0.10	4.06	3.46	10.86	8.04
CaO	8.23	5.10	2.40	5.20	1.29	8.99	6.97	9.56	8.64	2.67	0.60	6.67	13.76	12.28	11.78
Na2O	3.70	3.52	4.55	4.27	3.90	2.36	4.21	3.05	3.63	5.25	3.93	3.63	1.48	0.99	1.05
K2O	1.07	2.60	1.84	1.77	5.88	0.69	1.11	1.14	0.56	0.88	2.88	1.18	0.26	0.71	0.59
P2O5	0.20	0.34	0.07	0.20	0.11	0.22	0.28	0.19	0.42	0.01	0.03	0.24	0.18	0.24	0.16
LOI	0.72	0.88	0.49	1.01	0.16	0.39	0.85	1.16	0.64	0.57	0.98	0.75	0.60	0.76	0.53
Total	100.00	100.00	100.00	100.00	100.00	100.00	100.00	100.00	100.00	100.00	100.00	100.00	100.00	100.00	100.00
Trace elements															
Ba	235	665	592	478	2360	219	235	185	404	346	2038	625	112	150	127
Rb	8	70	35	46	66	1	18	25	10	14	52	40	4	9	7
Sr	420	684	256	955	385	327	253	372	376	276	157	335	574	326	439
Y	40	17	23	15	12	45	27	18	23	8	9	30	32	29	23
Zr	115	166	231	228	112	176	91	53	107	88	51	213	166	85	74
Nb	6	5	7	3	2	7	4	1	2	1	6	7	15	4	3
Th	1	5	6	6	8	3	1	1	0	6	10	5	2	1	1
Pb	6	4	8	11	24	**nd**	8	6	12	22	23	3	3	4	**nd**
Ga	10	13	6	13	8	12	12	8	11	5	8	7	6	6	5
Zn	182	83	21	54	15	132	194	169	95	**nd**	4	31	44	94	86
Cu	4	14	5	13	4	36	14	1	7	7	6	7	10	12	15
Ni	12	24	15	25	12	62	22	14	22	11	16	57	38	60	15
V	189	154	17	90	6	516	320	265	231	12	5	158	75	340	301
Cr	77	98	37	100	34	144	99	82	142	9	42	223	93	277	90
Sc	33	15	9	14	3	53	36	32	40	5	1	22	17	64	44
Co	15	15	**nd**	6	**nd**	44	22	25	30	0	**nd**	9	10	40	29
S	**nd**	120	**nd**	**nd**	**nd**	**nd**	1463	**nd**	**nd**	**nd**	**nd**	1476	**nd**	**nd**	875
La	11	22	13	22	21	7	23	22	18	20	24	20	31	5	6
Ce	**nd**	**nd**	**nd**	18	**nd**	**nd**	**nd**	**nd**	**nd**	**nd**	**nd**	**nd**	14	**nd**	**nd**
Nd	**nd**	**nd**	**nd**	**nd**	**nd**	**nd**	**nd**	**nd**	**nd**	**nd**	**nd**	**nd**	**nd**	**nd**	**nd**
Norm	E85	E86	SA15a	SA22	SA19	E81	SA8b	SA19x	SA21	E94H	SA4F	SA28	SA4A'	E94T	E94H'
Q (S)	10	11	34	13	23	7	1	1	3	36	39	22	31	7	11
or (KAS6)	6	16	11	11	35	4	7	7	3	5	17	7	2	4	4
ab (NAS6)	32	30	39	36	33	20	36	26	31	45	34	31	13	8	9
an (CAS2)	20	21	11	22	6	20	23	33	22	12	3	14	28	25	31
C(A)	0	0	0	0	1	0	0	0	0	0	6	0	0	0	0
Di wo(CS)	9	1	0	1	0	10	4	6	8	1	0	7	10	15	11
Di en(MS)	7	1	0	1	0	8	4	5	7	1	0	6	9	13	10
Hy en(MS)	7	11	3	10	1	10	11	10	12	1	0	4	0	15	11
mt(FF)	1	0	0	0	0	1	1	1	1	0	0	1	0	1	1
he(F)	8	7	2	5	1	18	11	11	11	1	1	6	4	11	12
ap(CP)	0	1	0	0	0	0	1	0	1	0	0	1	0	1	0
Totals	99	99	100	99	100	98	99	99	99	100	100	99	96	99	99

8.1. *Orthogneisses*

A total of 19 analyses were conducted on 19 zircon crystals for the sample SA15. Zircon grains are characterized by idiomorphic morphology with concentric zoning, although some have unzoned homogenous cores (Fig. 8a). The analyzed spots have U contents of 181–614 ppm, Th contents of 107–501 ppm, and Th/U ratios of 0.372–0.816 with an average of 0.663. Most of the analyzed zircons have Th/U ratios $\geq$ 0.5. It could verify their magmatic origin and crystallized from a high-siliceous magma (Kirkland et al., 2015) (Supplementary Table S9). The U-Pb isotopic analyses yield a weighted mean $^{206}Pb/^{238}U$ age of 994 $\pm$ 6 Ma (MSWD = 1.6) (Fig. 8a).

The separated zircons from sample SA2 are mostly euhedral to subhedral, stubby prismatic to equant (50–200 μm). Cathodoluminescence (CL) images show that the zircons of this sample display more complex internal structures with well-developed oscillatory zoning evident in other crystals with multiple stages of zircon crystallization and its primary magmatic origin (Corfu et al., 2003; Barth and Wooden, 2010) (Fig. 8b). Nineteen analyses were performed on 19 grains (Supplementary Table S10). U contents vary from 88 to 534 ppm, Th contents range from 47 to 577 ppm, and the Th/U ratio ranges from 0.179 to 0.728 except for one analysis, which recorded 1.306. The analyses yield a Concordia age of 976.6 $\pm$ 6.2 Ma (Fig. 8b) based on a group of concordant and equivalent analyses (MSWD = 0.95).

Zircon grains from sample SA18 are subidiomorphic and prismatic, with lengths ranging from 50 to 150 μm. These grains commonly have well-developed concentric oscillatory zoning, although some have unzoned homogenous cores (Fig. 8c). For sample SA18, 17 analyses were conducted on 17 grains. These analyses have U contents of 46–452 ppm, Th contents of 18–278 ppm, and Th/U ratios of (0.396 – 0.746) (Supplementary Table S9). The analyses yield a coherent Concordia age of 740 $\pm$ 6.4 Ma (Fig. 10c; 95% conf., MSWD = 1.06).

Zircons in the orthogneiss sample SA17X are usually euhedral, prismatic, and elongated crystals with sizes ranging from 50 to 200 μm. In CL images, they partially display well-developed oscillatory zoning, but other grains show only faint and broad zoning (Fig. 8d). A total of 18 analyses were performed on 18 zircon grains (Supplementary Table S9). The U content ranges from 95 to 815 ppm, the Th content from 34 to 421 ppm, and the Th/U ratio from 0.131 to 0.918 with an average of 0.441. The mean age of the zircons yields an age of 619.4 $\pm$ 4.2 Ma (Fig. 8d; MSWD = 0.0015).

A total of 19 analyses were conducted on 19 zircon grains from

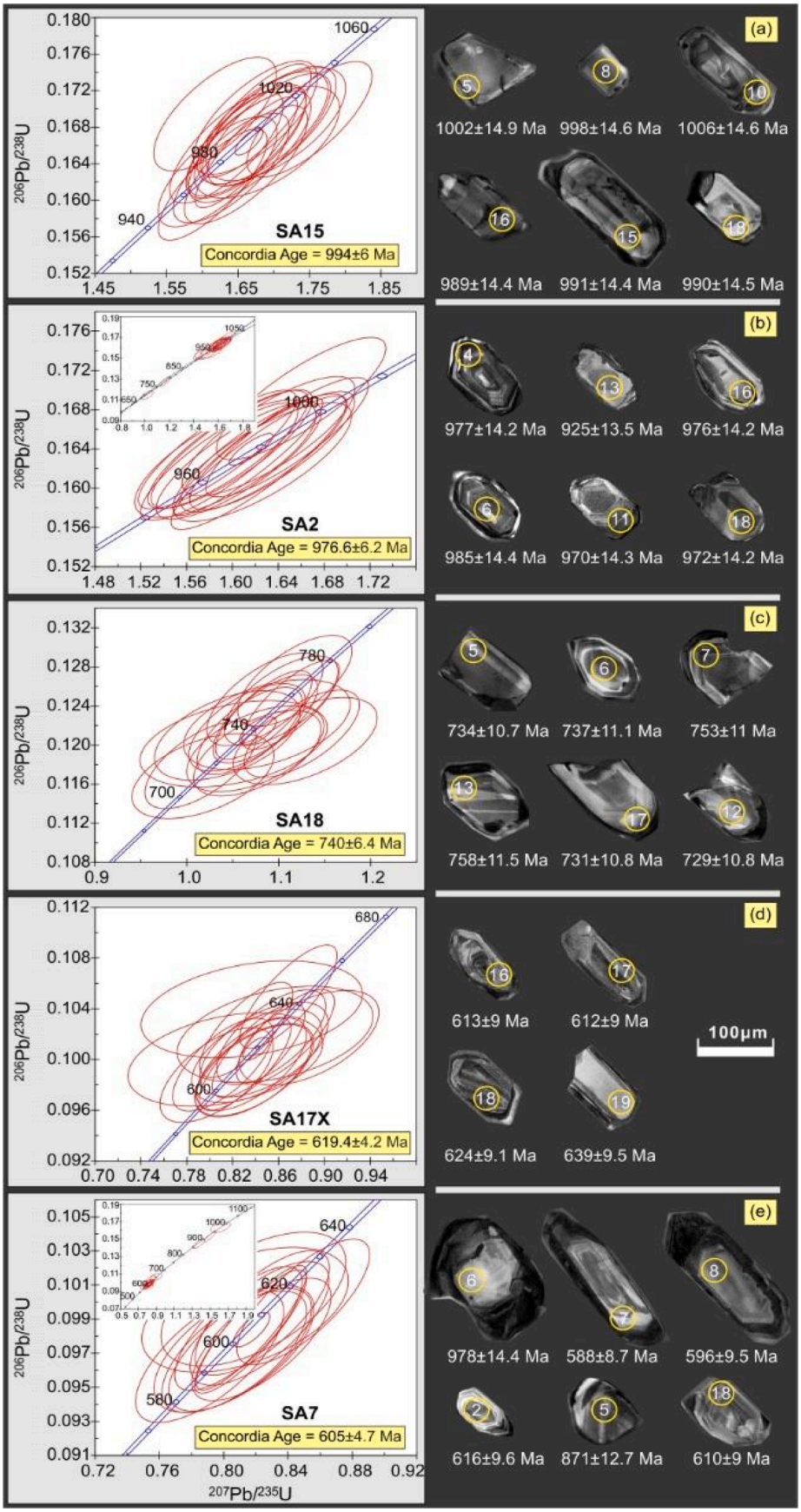

Fig. 8. Concordia plots and Cathodoluminescence (CL) images for magmatic zircon grains from orthogneisses.

sample SA7. Most zircon grains are euhedral to subhedral prismatic crystals with concentric zoning in cathodoluminescence images, but anhedral and rounded crystals are also observed (Fig. 8e). U contents vary from 94 to 605 ppm except for 3 spots that record high U contents (1105, 1232, and 2536 ppm), Th contents from 22 to 764 ppm and Th/U ratio range from 0.076 to 0.806. One analysis (SA7@16) is discordant, and yielding a younger age of 558 Ma. The remaining 18 concordant analyses yield a Concordia age of 605 ± 4.7 Ma (MSWD = 0.76, Fig. 8e; Supplementary Table S10).

8.2. *Paragneisses*

Zircon grains from sample SA4D are mostly anhedral to subhedral, prismatic to equant, and sometimes rounded. Their lengths range from 50 to 200 μm, and inherited cores are abundant (Fig. 9c). A total of 19 analyses were performed on 19 zircon grains (Supplementary Table S10). The U content varies from 150 to 1555 ppm, except for two spots that have U contents of 2247 ppm and 4126 ppm. The Th contents range from 70 to 627 ppm, except for four analyses with values 1059, 1334, 1952, and 3234 ppm. The Th/U ratio ranges from 0.39 to 0.979,

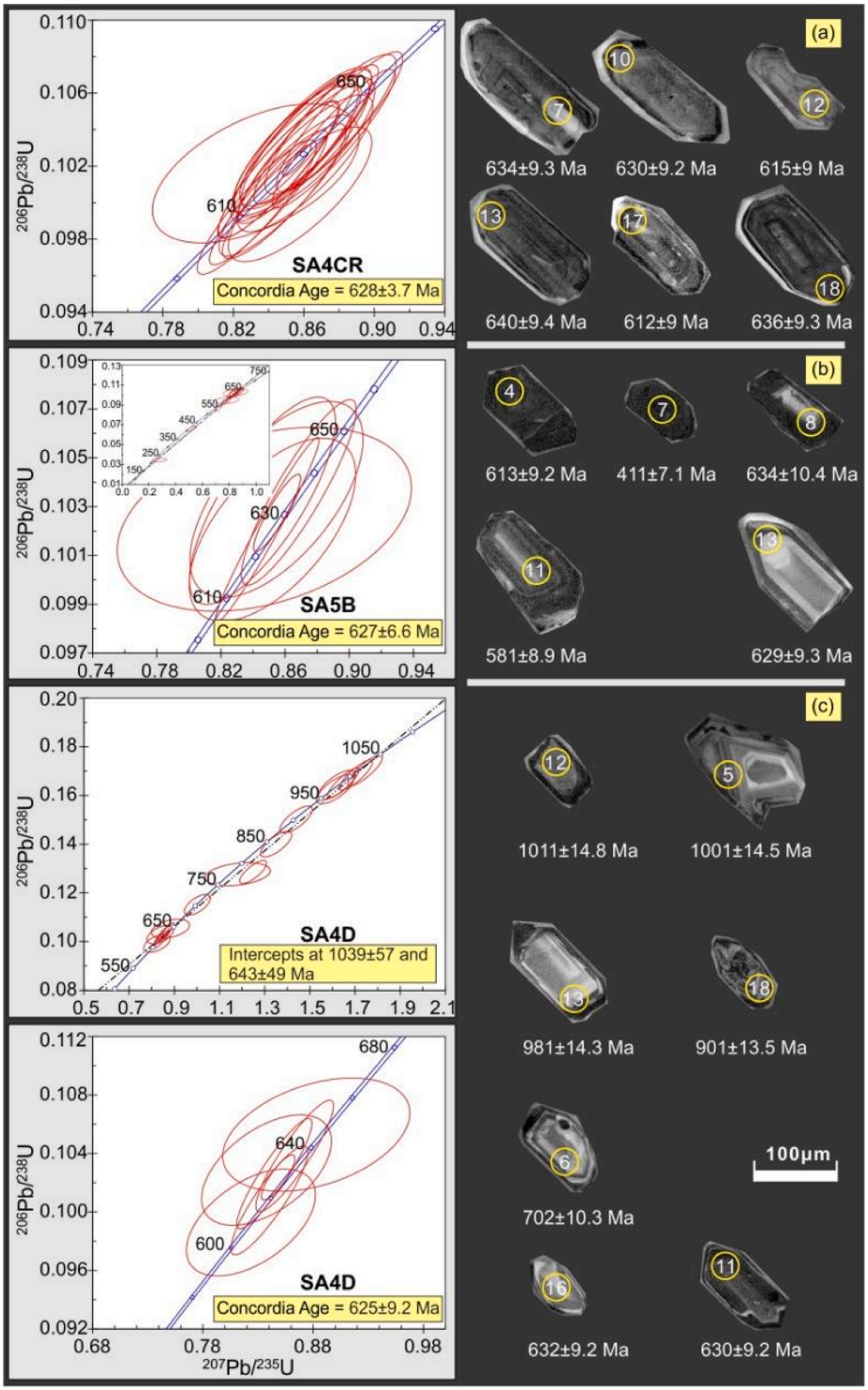

Fig. 9. Concordia plots and Cathodoluminescence (CL) images for detrital zircon grains from paragneisses.

except for one analysis with a ratio of 1.255. Data are plotted (Fig. 9c) along Concordia and define a wide range of ages. The Concordia line yields an upper intercept of 1039 ± 57 Ma (MSWD = 1.6) and a lower intercept of 643 ± 49 Ma. The U-Pb isotopic analyses of this sample yield a Concordia age of 625.1 ± 9.2 Ma (Fig. 9c).

Zircon grains from sample SA4CR have an equant to sub-rounded morphology and a size of about 100–150 μm (Fig. 9a). In cathodoluminescence (CL) images, zircon grains show relatively anhedral to subhedral rims and exhibit well-preserved concentric oscillatory growth structures. Twenty analyses of the same sample were conducted on 20 grains (Supplementary Table S10). These analyses have variable U contents of 233–1107 ppm, Th content is in the range of 114–532 ppm, except for one spot that has a content of 1462 ppm. The Th/U ratio is high (0.4– 0.619 with an average of 0.527), suggesting that these zircons are most likely magmatic in origin (Hoskin and Schaltegger, 2003). The U-Pb isotopic analyses yield a weighted mean age of 628 ± 3.7 Ma (MSWD = 0.00032) (Fig. 9a).

The zircon grains of the paragneiss sample (SA5B) show a large variation in their morphology and grain sizes. The shape of the zircon grains varies from equant to stubby, and some of them are rounded, with a size range from 50 to 150 μm. Some crystals in this sample are affected by intense metamictization. The U-Pb zircon analyses of the sample (SA5B) were performed at 16 analytical points on 16 grains. The U-Pb results of the analyses are listed in (Supplementary Table S9). Th and U content vary widely from 90 to 15363 ppm and from 49 to 98188 ppm, respectively. The Th/U ratio varies from 0.077 to 1.191, with an average of 0.688. The U-Pb isotopic analyses yield a weighted mean $^{206}Pb/^{238}U$ age of 627.2 ± 6.6 Ma (MSWD = 3.1) (Fig. 9b). Some analyses were excluded from the age calculation because they revealed significant uncertainties due to Pb loss in the high-U grains.

9. Discussion

In the following sections, the different field, petrological observations, geochemical, and geochronological data will be discussed in order to reveal the crystallization, depositional, and metamorphic history of the studied rocks. Then our data will be discussed within the frame of existing data from southern Sinai in order to get a robust tectonic model that may explain the tectonic evolution of the study area.

9.1. Mineral paragensis

On the basis of the petrographic relations between the mineral phases of the orthopyroxene-free paragneisses, four mineral assemblages could be defined. The first assemblage occurs as inclusions in the garnet porphyroblasts and is represented by a mineral assemblage of qz + pl ± mu ± chl + mt + apat. Since these inclusions are stable with the garnet core, we assume that the garnet core is part of the first assemblage. The second assemblage is represented by garnets mantel + qz + pl + bi + mu + mt + ilm ± spl. This assemblage represents the peak metamorphism and includes melt as observed from the field. The peak assemblage broke down into cd + bi + mu (third assemblage). The third assemblage is in equilibrium with the garnet (rim). Chlorite and sericite are the characteristic minerals for retrograde assemblage (the fourth assemblage).

One assemblage is observed in the orthopyroxene-bearing paragneisses, which is represented by opx + cpx + ksp + pl + gr + mt + ilm + melt ± qz ± Hb.

Two assemblages are observed in orthogneisses. The old and the main assemblage is represented by pl + qz ± Hbl ± bi + iron oxide ± apatite. The main assemblage is highly retrogressed to chlorite and sericite (i.e., the second assemblage).

9.2. Crystallization and intrusion of the protoliths of the orthogneisses/ortho-amphibolite

The geochemical data for both orthogneisses indicate that the protoliths were tonalite–trondhjemite–granodiorite, syenogranite, and granite in composition (Fig. 10a and b). The protolith of orthogneisses has calc-alkaline affinity, except for one sample (SA19) with alkaline affinity, as shown on the SiO_2-Alkalinity ratio diagram of Wright, 1969 (Fig. 10c). The orthogneisses are metaluminous, except one sample is peraluminous (SA19), according to the molar A/CAN versus A/NA diagram of Maniar and Piccolo, 1989 (Fig. 10d). The chemical data of the orthogneisses were plotted on the Na_2O versus K_2O diagram of Kleemann and Twist (1989) to differentiate the magma type for the protoliths. The Na_2O versus K_2O diagram shows an I-type character for the studied samples (Fig. 10e). By plotting these gneisses into the Nb versus Y diagram of Pearce et al. (1984), a volcanic arc syncollision setting is indicated for their protoliths (Fig. 10f).

The geochemical data of *ortho*-amphibolite were plotted on Na_2O/Al_2O_3 versus K_2O/Al_2O_3 diagram of Garrels and Mackenzie (1971) to check the igneous origin of the studied amphibolite. All plots fall within the field of igneous origin (Supplementary Fig. 3a). The chemical composition of the *ortho*-amphibolites suggests that their protoliths were basalts with sub-alkaline affinity (SiO_2 versus Zr/Ti diagram, Supplementary Fig. 3b). The tholeiitic nature of the protolith was confirmed by the relation between FeOt/MgO and SiO_2 (according to Miyashiro, 1975, Supplementary Fig. 3c). The data fall well within the mid-ocean-ridge basalt field on the Ti–Zr–Y ternary diagram (Pearce and Cann, 1973, Supplementary Fig. 3d) which may derived from back arc basin.

9.3. Depositional environment of the paragneisses and para-amphibolite

To study the protolith's nature in both paragneisses and *para*-amphibolite, the chemical analyses were plotted in the log $Fe_2O_3(t)/K_2O$ versus log SiO_2/Al_2O_3 diagram (Herron, 1988). The plot indicates that the paragneisses were derived from Fe-sand and arkose, whereas the *para*-amphibolite originated from Fe-shale (Supplementary Fig. 3e). Sedimentary basins can form in a variety of tectonic environments, including oceanic island arcs, continental island arcs, active and passive continental margins, collisional settings, and rift settings (Bhatia and Crook, 1986). The log K_2O/Na_2O vs. SiO_2 diagram of Roser and Korsch (1986) indicates that the sedimentary protoliths of *para*-amphibolite were deposited in an oceanic island arc margin, whereas the protoliths of paragneisses were deposited in a tectonic setting merging between an ocean island arc and active continental margin (Supplementary Fig. 3f).

9.4. Interpretation of U-Pb zircon data

The presented zircon geochronological data provide information about the time of magmatism, metamorphism, and the deposition ages of these rocks.

9.4.1. Orthogneisses

Old ages have been obtained from two orthogneiss samples (i.e., SA15 and SA2). Zircon extracted from these two samples yielded a Concordia age of 994 ± 6 Ma and 976.6 ± 6.2 Ma, respectively. The orthogneiss sample (SA18) shows a younger age of 740 ± 6.4 Ma, while the orthogneiss sample (SA17X) yielded a Concordia age of 619.4 ± 4.2 Ma, and sample (SA7) yielded a Concordia age of 605 ± 4.7 Ma.

Zircon grains extracted from orthogneiss samples (SA15 and SA2) are magmatic, and their ages are interpreted to represent the crystallization ages of an arc protolith. These ages are similar to U–Pb ages of 993 ± 11 and 1000 ± 4 Ma of biotite-orthogneisses in the Solaf area (Abu El-Enen and Whitehouse, 2013) and 977 ± 7 Ma of Sa'al tonalitic gneiss (Eyal et al., 2014).

Sample (SA18) yields a younger age of 740 ± 6.4 Ma, which is interpreted as the crystallization age of a younger arc (i.e., second arc).

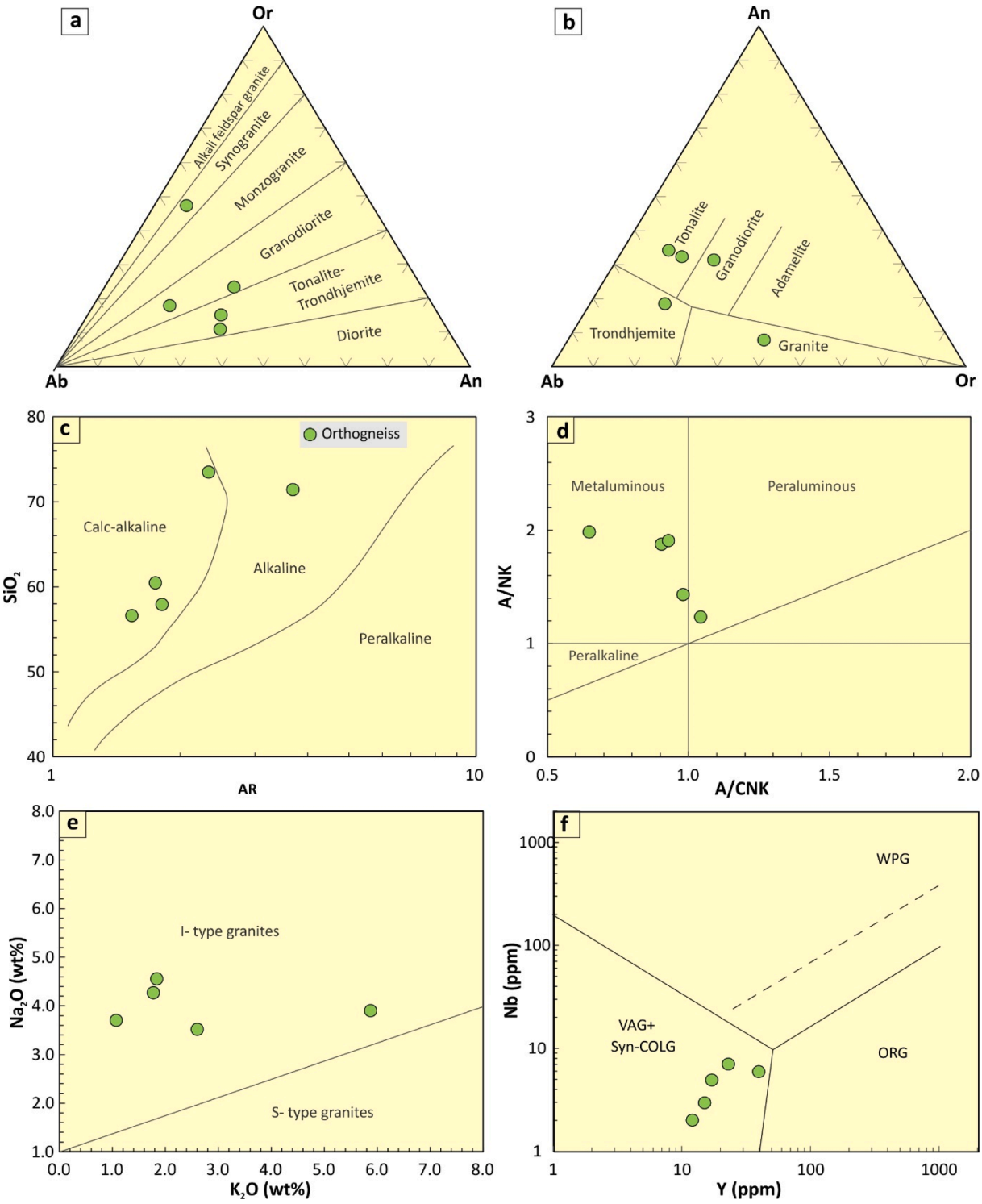

Fig. 10. (a) Normative Or-Ab-An ternary classification diagram (Streckeisen, 1976), (b) Normative An –Ab –Or classification diagram (O'Connor,1965), (c) A.R. vs SiO_2 diagram where A.R. (alkalinity ratio) = $[Al_2O_3 + CaO + (Na_2O + K_2O)]/[Al_2O_3 + CaO-(Na_2O + K_2O)]$ (wt.% ratio) (Wright, 1969), (d) Molecular ratio A/CNK $[Al_2O_3/(CaO + Na_2O + K_2O)]$ vs. Molecular ratio A/NK $[Al_2O_3/(Na_2O + K_2O)]$ binary diagram (Maniar and Piccolo, 1989), (e) Na_2O versus K_2O binary diagram (Kleemann and Twist, 1989), (f) Nb versus Y tectonic discrimination diagram (Pearce et al., 1984).

This age is correlated to the age of Taba granite gneiss (the northern part of the Taba Metamorphic Complex), which yielded zircon U–Pb ages of 737 ± 9 Ma (Kolodner, 2007).

There is another younger age (i.e., 619.4 ± 4.2 Ma) recorded for sample SA17X, which is interpreted to represent the crystallization age of a third island arc. A similar age (i.e., 622 ± 3 Ma) was recorded from quartz dioritic gneiss of the northern Kid Metamorphic Complex and was interpreted as the crystallization age of the granodiorite pluton (Eyal et al., 2014). The protolith of the biotite hornblende gneiss of the Feiran area crystallized at around 623 ± 6 (Abu El-Enen and Whitehouse, 2013), which is comparable to the suggested age of the third arc in the study area.

The younger age (605 ± 4.7 Ma) of the orthogneiss sample (SA7) is difficult to explain and ~~is~~ unacceptable since this rock unit is intruded by

617 ± 19 Ma gabbro (Abu Anbar, 2009). Thus, the more realistic for this age may represent Pb loss events.

9.4.2. *Paragneisses and depositional age*

The paragneiss sample (SA4D) gave two different ages; the oldest age is 1039 ± 57 Ma, and the youngest age is 643 ± 49 Ma. On the other hand, the other two samples (SA4CR and SA5B) yielded a single-age population, with a Concordia age of 628 ± 3.7 Ma and 627 ± 6.6 Ma, respectively. CL imaging reveals oscillatory zoning in these zircon grains, indicating that they are of igneous origin. Additionally, their subhedral morphologies imply that the immature sediments were transported over short distances from their igneous source region to the depositional environment.

The oldest ages (1039 ± 57 Ma) recorded for the sample (SA4D) are comparable to ages recorded in Sinai and the Eastern Desert basement. Ages from gneiss domes such as Hafafit, Meatiq, El-Shaloul, and El-Sibai yield ages<800 Ma (e.g., Andresen et al., 2009, have been dated the gneissose granites of the Sikait area at 677 Ma, Augland et al., 2012, concluded that the crystallization ages of orthogneiss protoliths of El-Sibai gneiss are 685–679 Ma, Ali et al., 2015, reported the granitoid gneisses of Wadi Beitan at 744–719 Ma, Abu El-Enen et al., 2016, presented U-Pb data that yields 731 ± 3 Ma for the biotite-hornblende gneiss protolith). Similar ages are recorded in Sinai (1045—1025 ± 13 Ma) for the old island arc crust that formed Moneiga quartz-diorite that is located within the Katherine ring complex (Bea et al., 2009). These old ages of the paragneisses were interpreted to date the crystallization ages of magmatic arc rocks forming the sedimentary precursor of the paragneisses.

Detrital zircon geochronology can provide important constraints on the maximum age of deposition of the host sediments. The ages of the youngest concordant detrital zircons confine the depositional ages of paragneisses (e.g., Collins et al., 2003). U–Pb zircon dating of the studied paragneisses indicates a maximum depositional age for the last cycle of 625 ± 9.2 Ma for their immature sedimentary protolith.

The depositional ages of Sinai are vast and cover a wide range of ages, which reflect the complicated tectonic history of the Sinai Peninsula. Moghazi et al. (2012) dated detrital zircons from Um Zariq metasediments (Kid Metamorphic Complex) and concluded that the maximum and minimum depositional ages were 813 ± 16 Ma and 647 ± 12 Ma, respectively. Eyal et al. (2014) have proposed a maximum depositional age for the Um Zariq schists of 730 Ma, 800 Ma for the Taba schist, and 790 Ma for the Taba gneiss. Zaghra Formation was deposited and deformed between 625 and 615 Ma (Andresen et al., 2014). Abu El-Enen and Whitehouse (2013) concluded that the depositional age of the Feiran-Solaf protolith sediments lasted until 660 Ma, and the sediments came from a variety of sources with different ages. U-Pb zircon geochronology of the volcano-sedimentary association of the Hafafit metamorphic complex indicates a maximum sedimentation age is 651 ± 2 Ma (Abu El-Enen et al., 2016).

The protoliths of the orthogneisses were volcanic arc (Fig. 10f). The ages of these different arc protoliths of orthogneisses overlap the ages of paragneisses (Fig. 11), which may indicate that the provenance of the detrital zircon may be derived from successive arcs with different ages. Abu El-Enen and Whitehouse (2013) proposed that the 1000 Ma detrital zircon of Feiran-Solaf could have come from a nearby source area, which has a similar Grenvillian-age crust (Be'eri-Shlevin et al., 2012; Eyal et al., 2014).

9.4.3. *Metamorphism-age and condition*

Metamorphic ages from the Sinai crystalline metamorphic rocks imply 4 metamorphic events. According to Abu Anbar et al. (2004), the first event took place at 838 ± 16 Ma for Feiran gneisses and was interpreted as the age of gneisses formation. The second event (800–650 Ma) was proposed by some authors, such as Eyal et al. (2014), who suggested that the second age peak (i.e., 768 ± 5 Ma and 720 ± 8 Ma) coincides with the high-temperature metamorphism of Qenaia migmatitic gneisses in the Kid Metamorphic Complex and Sa'al granite-quartz monzonite gneisses, respectively. Blasband et al. (2000) proposed a *syn*-prograde greenschist metamorphism in the Kid Metamorphic Complex at 720–650 Ma to be due to arc-accretion processes. Old metamorphic age (713 ± 14 Ma) is also documented via U–Pb geochronology of monazite in the Taba Metamorphic Complex migmatites (Elisha et al.,

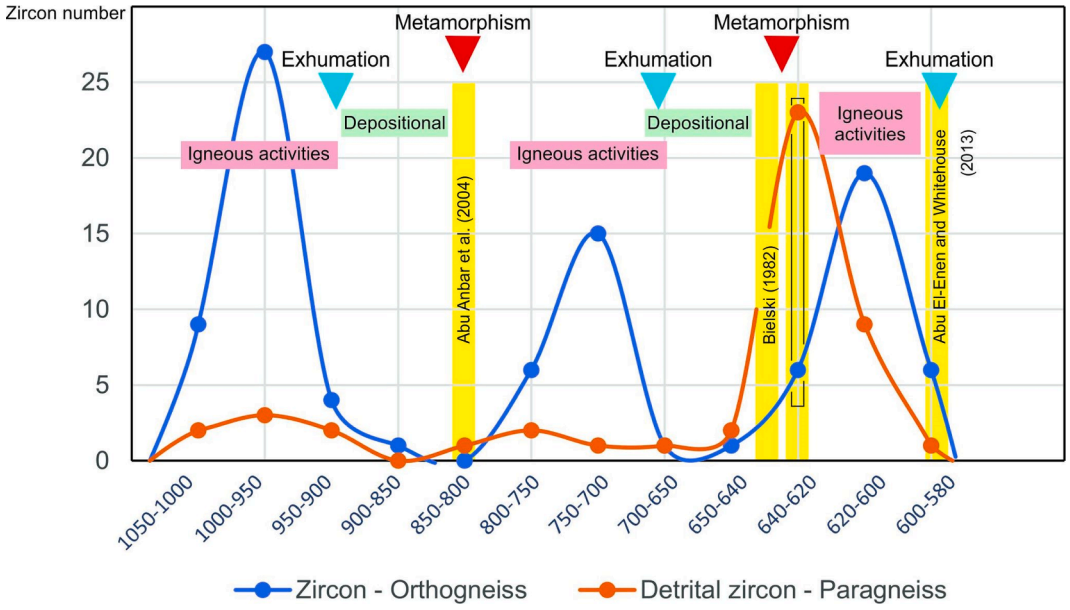

Fig. 11. Illustrates the age distribution of zircon and detrital zircon within the study area, based on the data provided in the present contribution. Zircon data extracted from orthogneisses are indicative of igneous activities, while detrital zircon obtained from paragneisses signal cycles of deposition. Notably, it should be highlighted that the ages of the detrital zircons closely mirror those of the igneous zircons, suggesting that the sources of the detrital zircons are the orthogneisses. For instance, the highlighted rectangle spanning 640–620 demonstrates a prominent detrital zircon peak aligned with its corresponding igneous signature. The occurrence of each metamorphic event (depicted by yellow bars) is followed by subsequent igneous activity and exhumation cycles, thereby enabling erosion to take effect and resulting in the deposition of new sediments that serve as the source for the paragneisses.

2019).

The third event (650——630 Ma) was recorded in different areas of Sinai. Bielski (1982) deduced Rb-Sr ages for the formation of the Feiran-Solaf Metamorphic Complex gneisses at 643 ± 41 Ma. Stern and Manton (1987) proposed that the peak metamorphic conditions in the Feiran-Solaf Metamorphic Complex occurred at 632 Ma. According to Abu El-Enen and Whitehouse (2013), the peak regional metamorphism at upper amphibolite facies conditions of the Feiran-Solaf Metamorphic Complex occurred approximately at 627 ± 7 Ma. Our data (i.e., 633 ± 10 Ma depending on the low Th/U ratios < 0.1; Hoskin and Schaltegger, 2003) indicate that the metamorphism at the Seih area is equivalent to the third peak and metamorphism recorded elsewhere in Sinai.

The fourth metamorphic event (620——590 Ma) was recorded in Wadi Kid area. Cosca et al. (1999) reported a peak regional metamorphism at Kid Metamorphic Complex that was thought to have occurred at around 620 ± 10 Ma. Blasband et al. (2000) proposed that peak regional metamorphism in Kid Metamorphic Complex occurred between 620 and 600 Ma as a result of the intrusion of granitic magma caused by a regional extension (Shimron, 1985; Reymer and Oertel, 1985; Blasband et al., 1997). The volcano-sedimentary sequence of the Janub Metamorphic Complex (JMC) regionally metamorphosed at lower green schist facies conditions between 618 and 615 Ma (Ghanem et al., 2022). Abu El-Enen and Whitehouse (2013), concluded that the age 592 ± 10 Ma was thought to be connected to a shallow crustal-level isothermal decompression metamorphic cooling event of the Feiran-Solaf Metamorphic Complex. Most of these later metamorphic events were associated with ductile deformation (Fowler et al., 2010; Abu El-Enen, 2011). This fourth metamorphic event is observed in the Seih area, causing ductile deformation in the orthogneisses, which was recorded at 620 Ma.

Different geothermobarometers indicate that orthopyroxene-free paragneisses metamorphosed in a temperature range from 550 to 775 °C and 3–5 kb of pressure, while the orthogneisses metamorphosed at 530 to 760 °C and 4–7 kb. Field observations (e.g. presence of leucosome) confirm these relatively high grade metamorphism (Fig. 4a). The highest temperature (870 °C) was recorded for orthopyroxene-bearing paragneisses at a pressure of 5–7 kb. Some of the earlier studies are close to our findings, e.g., El-Tokhi, 2003; Eliwa et al., 2008; Abu El-Enen et al., 2009, which suggested that the metamorphic rocks of the Feiran–Solaf Complex were subjected to a single regional metamorphism with peak metamorphic conditions of 600–700 °C and P < 5 kb. Abu-Alam and Stüwe, 2009; Abu El-Enen, 2011, suggested a single clockwise P–T path for gneisses and metapelites in the Feiran-Solaf Metamorphic Complex with peak metamorphic conditions around 7–8 kb and 700–750 °C, followed by isothermal decompression to about 4–5 kb at higher a temperature, attaining 770–785 °C, and finally near isobaric cooling to 450 °C.

9.5. *Regional implication*

Zircon's U-Pb age date of the studied orthogneisses indicates that Wadi Seih area was subjected to at least three igneous activities (Fig. 11). The geochemistry of orthogneisses indicates three arcs (Fig. 10f) and is evidenced by three zircon age populations.

9.5.1. *Rodinia assembly*

The oldest population of the orthogneisses is from 1050 to 900 Ma, with a major peak at ca. 1000 Ma. The 1000 Ma may be attributed to Grenvillian-age crust (ca. 1300–1000 Ma; Li et al., 2008) that has been documented in numerous areas within the ANS (Hargrove et al., 2006; Avigad et al., 2007; Abu El-Enen and Whitehouse, 2013; Abu-Alam et al., 2014; Hassan et al., 2020). This age may mark the final stage of the assembly of the Late Mesoproterozoic-Early Neoproterozoic supercontinent of Rodinia (Be'eri-Shlevin et al., 2009a, b, 2012).

9.5.2. *Break up of Rodinia*

A recorded age gap (i.e. 900—850 Ma) was observed in the presented data (Fig. 11). This age gap could be interpreted as a break up of Rodinia and formation of Mozambique ocean (Meert and Torsvik, 2003; Fritz et al., 2013; Hassan et al., 2020) or as long-term passive margins for the region (Bradley, 2008). Ophiolitic rocks in central and southern Eastern Desert assign ages from 890 to 690 Ma (Stern et al., 2004) and probably formed within the Mozambique ocean (Stern, 1994; Azer, 2014). As a result, we prefer to follow the former suggestion i.e., the recorded age gap represents the break up of Rodinia.

9.5.3. *Closure of Mozambique ocean and Gondwana assembly*

The second peak of zircon ages ranges from 850 to 700 Ma, with an average age of 750 Ma. This age population may reflect arc-arc convergence and terrane suturing, marking the beginning of ocean-basin closure and Gondwana assembly (Fritz et al., 2013; Abu-Alam et al., 2014; Hamimi et al., 2021). Similar ages were recorded in Sinai, such as 844 ± 4 Ma, from Moneiga quartz-diorites (Bea et al., 2009), 819 Ma of quartz monzonitic gneiss from Saal Metamorphic Complex (Be'eri-Shlevin et al., 2012), 792 ± 7 Ma of the foliated biotite-gneiss in the western margin of the Solaf zone (Abu El-Enen and Whitehouse, 2013), 782 ± 7 Ma reported from a slightly foliated granodiorite (Stern and Manton, 1987), 802 ± 6 Ma of quartz diorite and 785 ± 7 Ma of tonalitic gneiss of the Feiran-Solaf Metamorphic Complex (Eyal et al., 2014), 777 ± 4 Ma of Qenaia gneisses (Kid Metamorphic Complex) and 737 ± 9 Ma of Taba granitic gneiss (Kolodner, 2007). This peak corresponds well in age to the Feiran-Taba arc that formed between about 870 and 740 Ma (Eyal et al., 2014; Hassan et al., 2020).

9.5.4. *Peak amalgamation of Gondwana and metamorphism*

The third peak of zircon ages ranges from 650 to 580 Ma, with a major peak at 620 Ma. This age may be related to the peak amalgamation of Gondwana at ca. 630 Ma (Meert and Torsvik, 2003; Cawood, 2005; Collins and Pisarevsky, 2005; Cawood and Buchan, 2007). This age is similar to the crystallization ages of the Feiran biotite-hornblende gneisses (632 ± 3 and 623 ± 6; Stern and Manton, 1987; Abu El-Enen and Whitehouse, 2013) and the Ghurabi dioritic and Gnethel quartz dioritic gneisses of the Kid Metamorphic Complex (628 ± 4 and 622 ± 3 Ma; Eyal et al., 2014).

The present data suggested that the regional metamorphism occurred in this stage at 633 ± 10 Ma. The metamorphism of gneisses occured under amphibolite-facies conditions with temperatures range from 530 to 775 °C, while the orthopyroxene-bearing paragneisses were metamorphosed under granulite-facies at a temperature of 870 °C.

10. Tectonic model and conclusions

Based on the data presented in the current contribution within the frame of previously published data, we suggest the following tectonic model (Fig. 12) explain the evolution of Wadi Seih area.

Generally, we can recognize that the oldest arc in Wadi Seih area formed from 1050 to 900 Ma (Fig. 8a and b). This arc (Fig. 10f) could be related to the latest Mesoproterozoic ocean closure (Be'eri-Shlevin et al., 2012) during the assembly of the Rodinia supercontinent (1300 to 1000 Ma; Rogers and Santosh, 2002; Zhao et al., 2002; Li et al., 2008; Evans and Mitchell, 2011). At nearly 900 to 850, the rifting of the Rodinia supercontinent occurred (Fritz et al., 2013), and as a result, a new oceanic crust, i.e., the Mozambique Ocean (Stern, 1994; Meert and Torsvik, 2003), was developed. Shortly after the formation of the Mozambique Ocean, several subduction zones were initiated (780 Ma; Johnson and Woldehaimanot 2003), leading to the formation of volcanic arcs (i.e., the second arc, Fig. 8c) during the closing of the Mozambique Ocean and initiation of Gondwana assembly. At 650–600 Ma, the East-West Gondwana collision stage (third arc, Fig. 8d) occurred. This arc is related to the peak amalgamation of Gondwana (Meert and Torsvik, 2003; Cawood, 2005; Collins and Pisarevsky, 2005;

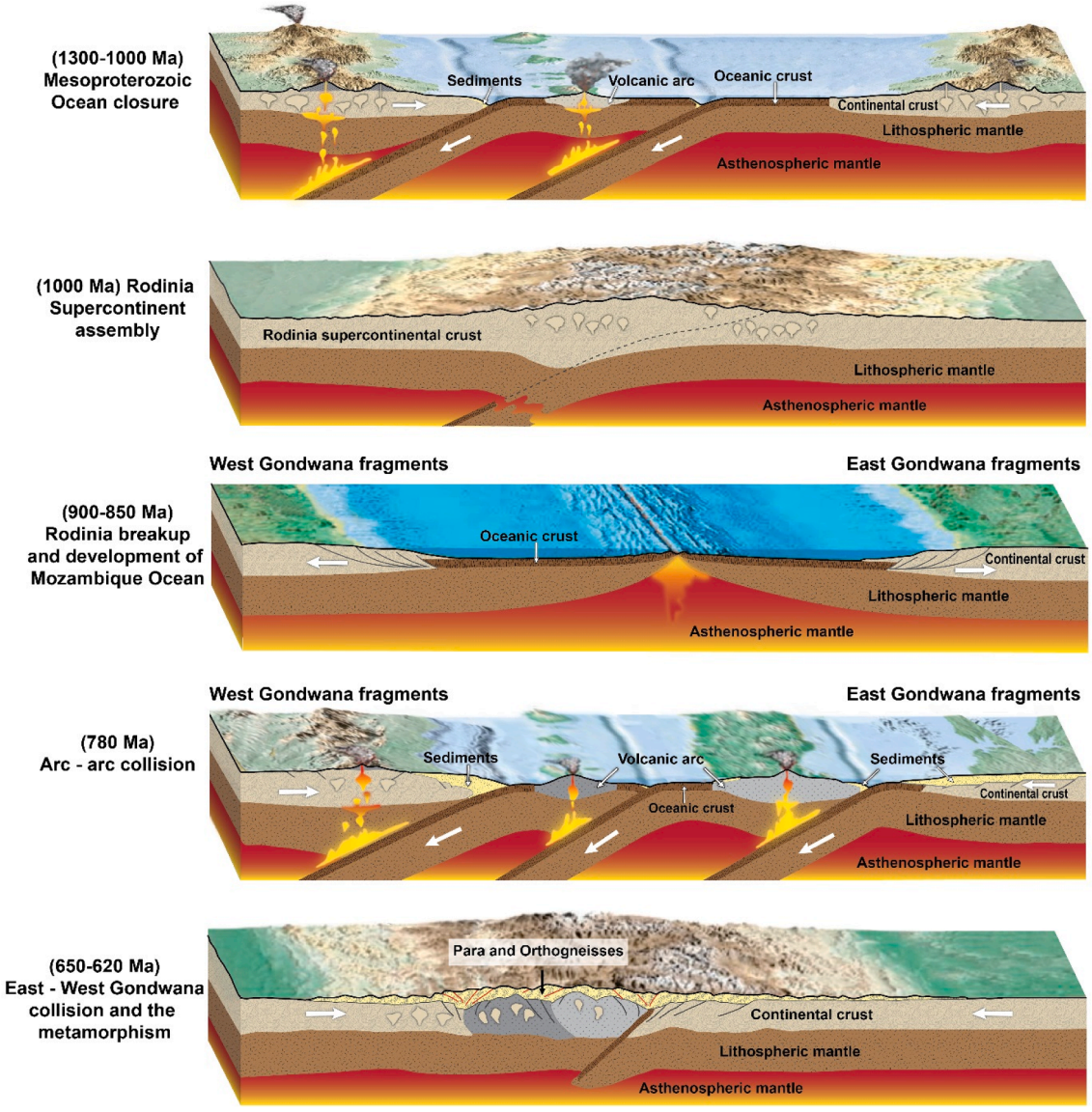

Fig. 12. A proposed schematic diagram for the tectonic evolution of Wadi Seih area. The initial diagram has been adapted from Lutgens et al., 2018. The model's ages and tectonic setting are grounded in the findings of the current study.

Cawood and Buchan, 2007). This collision is responsible for the peak metamorphism in Wadi Seih area.

Declaration of Competing Interest

The authors declare that they have no known competing financial interests or personal relationships that could have appeared to influence the work reported in this paper.

Data availability

Data will be made available on request.

Acknowledgment

We would like to express our sincere thanks to Prof. Ralf Kryza from Institute of Geological Sciences, Wroclaw University, Poland, for assistance to carry out the microprobe analyses. Grateful thanks also to Prof. Massimo Coltorti from Earth Science Department, Ferrara University, Italy, for analyzing major and trace elements.

Appendix A. Supplementary material

Supplementary data to this article can be found online at https://doi.org/10.1016/j.precamres.2023.107221.

References

Abu Anbar, M.M., 2009. Petrogenesis of the Nesryin gabbroic intrusion in SW Sinai, Egypt: new contributions from mineralogy, geochemistry, Nd and Sr isotopes. Mineral. Petrol. 95 (1), 87–103.

Abu Anbar, M., Abd El-Wahed, M., 2004. Geochemistry, mineralogy and evolution of Feiran gneisses and amphibolites, SW Sinai, Egypt. In Sixth inter Conf on geochemistry, Alexanderia Univ (Vol. 15, No. 16, pp. 747-776).

Abu Anbar, M., Solis Pichardo, G., Hernandez Bernal, M. S., 2004. Sm-Nd and Rb-Sr isotopes of Feiran gneisses and amphibolites: evidences of pre-Pan-African continental crust in Sinai, Egypt. 6th Inter. Conf. Geochem., Alex. Univ., Egypt, 727–745.

Abu Anbar, M., Finger, F., Solís Picharo, G., 2009. Evolution of the metamorphosed volcano-sedimentary rocks in Sa'al area, southern Sinai, Egypt: implications from lithology, geochemistry, mineralogy, P-T conditions and age dating, Egypt. J. Geol. 53, 1–3.

Abu El-Enen, M.M., 2011. Geochemistry, provenance, and metamorphic evolution of Gabal Samra Neoproterozoic metapelites, Sinai, Egypt. J. Afr. Earth Sci. 59, 269–282.

.

Abu El-Enen, M.M., Okrusch, M., Will, T.M., 2004. Contact metamorphism and metasomatism at a dolerite-limestone contact in the Gebel Yelleq area, Northern Sinai, Egypt. Mineralogy and Petrology 81, 135–164.

Abu El-Enen, M.M., Whitehouse, M.J., 2013. The Feiran-Solaf metamorphic complex, Sinai, Egypt: geochronological and geochemical constraints on its evolution. Precambr. Res. 239, 106–125.

Abu El-Enen, M.M., Zalata, A.A., Abd El-Shakour, Z.A., 2009. Subsolidus and anatectic migmatites: examples from the Pan-African crystalline basement, southern Sinai, Egypt. Egyptian J. Geol. 53, 63–86.

Abu El-Enen, M.M., Abu-Alam, T.S., Whitehouse, M.J., Ali, K.A., Okrusch, M., 2016. P-T path and timing of crustal thickening during amalgamation of East and West Gondwana: A case study from the Hafafit Metamorphic Complex, Eastern Desert of Egypt. Lithos 263, 213–238.

Abu-Alam, T.S., Hassan, M., Stüwe, K., Meyer, S.E., Passchier, C.W., 2014. Multistage tectonism and metamorphism during Gondwana collision: Baladiyah complex, Saudi Arabia. J. Petrol. 55 (10), 1941–1964.

Abu-Alam, T.S., Stüwe, K., 2009. Exhumation during oblique transpression: the Fieran-Solaf region, Egypt. J. Metamorphic Geol. 27, 439–459.

Ali, K.A., Kröner, A., Hegner, E., Wong, J., Li, S.Q., Gahlan, H.A., El Ela, F.F.A., 2015. U-Pb zircon geochronology and Hf–Nd isotopic systematics of Wadi Beitan granitoid gneisses, south Eastern Desert, Egypt. Gondw. Res. 27 (2), 811–824.

Allen, P.A., Eriksson, P.G., Alkmim, F.F., Betts, P.G., Catuneanu, O., Mazumder, R., Meng, Q., Young, G.M., 2015. Classification of basins, with special reference to Proterozoic examples. Geol. Soc. Lond. Mem. 43 (1), 5–28.

Andresen, A., El-Rus, M.A.A., Myhre, P.I., Boghdady, G.Y., Corfu, F., 2009. U-Pb TIMS age constraints on the evolution of the Neoproterozoic Meatiq Gneiss dome, Eastern Desert, Egypt. Int. J. Earth Sci. 98 (3), 481–497.

Andresen, A., Abu El-Enen, M.M., Stern, R.J., Wilde, S.A., Ali, K.A., 2014. The Wadi Zaghra metasediments of Sinai, Egypt: new constraints on the late Cryogenian-Ediacaran tectonic evolution of the northernmost Arabian-Nubian Shield. Int. Geol. Rev. 56 (8), 1020–1038.

Augland, L.E., Andresen, A., Boghdady, G.Y., 2012. U-Pb ID-TIMS dating of igneous and metaigneous rocks from the El-Sibai area: time constraints on the tectonic evolution of the Central Eastern Desert, Egypt. Int. J. Earth Sci. 101 (1), 25–37.

Avigad, D., Stern, R.J., Beyth, M., Miller, N., McWilliams, M.O., 2007. Detrital zircon U-Pb geochronology of Cryogenian diamictites and lower Paleozoic sandstone in Ethiopia (Tigrai): age constraints on Neoproterozoic glaciation and crustal evolution of the southern Arabian-Nubian Shield. Precambr. Res. 154, 88–106.

Azer, M.K., 2014. Petrological studies of Neoproterozoic serpentinized ultramafics of the Nubian Shield: spinel compositions as evidence of the tectonic evolution of Egyptian ophiolites. Acta Geol. Pol. 64 (1), 113–127.

Azer, M.K., Stern, R.J., Kimura, J.-I., 2010. Origin of a Late Neoproterozoic (605±13 Ma) intrusive carbonate-albitite complex in Southern Sinai, Egypt. Int. J. Earth Sci. 99, 245–267.

Barth, A.P., Wooden, J.L., 2010. Coupled elemental and isotopic analyses of polygenetic zircons from granitic rocks by ion microprobe, with implications for melt evolution and the sources of granitic magmas. Chem. Geol. 277 (1–2), 149–159.

Be'eri-Shlevin, Y., Katzir, Y., Whitehouse, M.J., 2009. Post-collisional tectono-magmatic evolution in the northern Arabian-Nubian Shield: time constraints from ion-probe U-Pb dating of zircon. J Geol Soc Lond 166, 71–85.

Be'eri-Shlevin, Y., Katzir, Y., Whitehouse, M.J., Kleinhanns, I.C., 2009. Contribution of pre-Pan-African crust to formation of the Arabian– Nubian Shield: new secondary ionization mass spectrometry U-Pb and O studies of zircon. Geology 37, 899–902.

Be'eri-Shlevin, Y., Samuel, M.D., Azer, M.K., Rämö, O.T., Whitehouse, M.J., Moussa, H. E., 2011. The Ediacaran Ferani and Rutig volcano-sedimentary successions of the northernmost Arabian-Nubian Shield (ANS): New insights from zircon U-Pb geochronology, geochemistry and O-Nd isotope ratios. Precambr. Res. 188, 21–44.

Bea, F., Abu-Anbar, M., Montero, P., Peres, P., Talavera, C., 2009. The~ 844 Ma Moneiga quartz-diorites of the Sinai, Egypt: evidence for Andean-type arc or rift-related magmatism in the Arabian-Nubian Shield? Precambr. Res. 175 (1–4), 161–168.

Be'eri-Shlevin, Y., Eyal, M., Eyal, Y., Whitehouse, M.J., Litvinovsky, B., 2012. The Sa'al volcano-sedimentary complex (Sinai, Egypt): a latest Mesoproterozoic volcanic arc in the northern Arabian Nubian Shield. Geology 40 (5), 403–406.

Bentor, Y.K., 1985. The crustal evolution of the Arabo-Nubian Massif with special reference to the Sinai Peninsula. Precambr. Res. 28 (1), 1–74.

Bhatia, M.R., Crook, K.A., 1986. Trace element characteristics of graywackes and tectonic setting discrimination of sedimentary basins. Contrib. Miner. Petrol. 92 (2), 181–193.

Bhattacharya, A., Mazumdar, A.C., Sen, S.K., 1988. Fe-Mg mixing in cordierite; constraints from natural data and implications for cordierite-garnet geothermometry in granulites. Am. Mineral. 73, 338–344.

Bhattacharya, A., Mohanty, L., Maji, A., Sen, S.K., Raith, M., 1992. Non-ideal mixing in the phlogopite-annite binary: constraints from experimental data on Mg-Fe partitioning and a reformulation of the biotite-garnet geothermometer. Contrib. Miner. Petrol. 111 (1), 87–93.

Bielski, M., 1982. Stages in the Evolution of the Arabian-Nubian Massif in Sinai. Hebrew University, Jerusalem, p. 155. Ph.D. Thesis.

Blasband, B., Brooijmans, P., Dirks, P., Visser, W., White, S., 1997. A Pan-African core complex in the Sinai, Egypt. Geol. Mijnb. 76 (3), 247–266.

Blasband, B., White, S., Brooijmans, P., De Boorder, H., Visser, W., 2000. Late Proterozoic extensional collapse in the Arabian-Nubian shield. J. Geol. Soc. London 157 (3), 615–628.

Blundy, J.D., Holland, T.J.B., 1990. Calcic amphibole equilibria and a new amphibole-plagioclase geothermometer. Contrib. Miner. Petrol. 104, 208–224.

Bradley, D.C., 2008. Passive margins through earth history. Earth Sci. Rev. 91 (1–4), 1–26.

Brooijmans, P., Blasband, B., White, S.H., Visser, W.J., Dirks, P., 2003. Geothermobarometric evidence for a metamorphic core complex in Sinai, Egypt. Precambr. Res. 123, 249–268.

Cathelineau, M., 1988. Cation Site Occupancy in Chlorites and Illites as a Function of Temperature. Clay Miner. 23, 471–485.

Cawood, P.A., 2005. Terra Australis Orogen: Rodinia breakup and development of the Pacific and Iapetus margins of Gondwana during the Neoproterozoic and Paleozoic. Earth Sci. Rev. 69 (3–4), 249–279.

Cawood, P.A., Buchan, C., 2007. Linking accretionary orogenesis with supercontinent assembly. Earth Sci. Rev. 82, 217–256.

Cawood, P.A., McCausland, P.J.A., Dunning, G.R., 2001. Opening Iapetus: constraints from the Laurentian margin of Newfoundland. Geol. Soc. Am. Bull. 113, 443–453.

Collins, A.S., Kröner, A., Fitzsimons, I.C., Razakamanana, T., 2003. Detrital footprint of the Mozambique ocean: U-Pb SHRIMP and Pb evaporation zircon geochronology of metasedimentary gneisses in eastern Madagascar. Tectonophysics 375 (1–4), 77–99.

Collins, A.S., Pisarevsky, S.A., 2005. Amalgamating eastern Gondwana: the evolution of the Circum-Indian Orogens. Earth Sci. Rev. 71 (3–4), 229–270.

Corfu, F., Hanchar, J.M., Hoskin, P.W., Kinny, P., 2003. Atlas of zircon textures. Rev. Mineral. Geochem. 53 (1), 469–500.

Cosca, M.A., Shimron, A., Caby, R., 1999. Late Precambrian metamorphism and cooling in the Arabian-Nubian Shield. Petrology and 40Ar/39Ar geochronology of metamorphic rocks of the Elat area (southern Israel). Precambr. Res. 98, 107–127.

Daly, M.C., Tozer, B., Watts, A.B., 2018. Cratonic basins and the Wilson cycle: a perspective from the Parnaíba Basin, Brazil. Geol. Soc. Lond. Spec. Publ. 470 (1), 463–477.

Dasgupta, P., 2020. Formation of intracratonic Gondwana basins: Prelude of Gondwana fragmentation? J. Mineral. Petrol. Sci. 115 (2), 192–201.

Dasgupta, S., Sengupta, P., Guha, D., Fukuoka, M., 1991. A refined garnet-biotite Fe− Mg exchange geothermometer and its application in amphibolites and granulites. Contrib. Miner. Petrol. 109 (1), 130–137.

Deer, W.A., Howie, R.A., Zussman, J., 1978. Rock-forming minerals. 2A, single chain silicates. Longman, London, 668 P.

Deer, W.A., Howie, A., Sussman, J., 1986. An interdiction to rock-forming minerals, 17th. Howie, J. Sussman-Longman Ltd.

Elisha, B., Katzir, Y., Kylander-Clark, A.R., Golan, T., Coble, M.A., 2019. The timing of migmatization in the northern Arabian-Nubian Shield: Evidence for a juvenile sedimentary component in collision-related batholiths. J. Metam. Geol. 37 (5), 591–610.

Eliwa, H.A., El-Enen, M.A., Khalaf, I.M., Itaya, T., Murata, M., 2008. Metamorphic evolution of Neoproterozoic metapelites and gneisses in the Sinai, Egypt: Insights from petrology, mineral chemistry and K-Ar age dating. J. Afr. Earth Sc. 51 (3), 107–122.

Elkins, L.T., Grove, T.L., 1990. Ternary feldspar experiments and thermodynamic models. Am. Mineral. 75 (5–6), 544–559.

El-Shafei, M.K., Kusky, T.M., 2003. Structural and tectonic evolution of the Neoproterozoic Feiran-Solaf metamorphic belt, Sinai Peninsula: implications for the closure of the Mozambique Ocean. Precambr. Res. 123 (2–4), 269–293.

El-Tokhi, M., 2003. Petrogenesis, geochemistry and origin of the Precambrian gneisses of Feiran Complex, south western Sinai, Egypt. Ann Geol Surv Egypt 26, 1–17.

El-Tokhi, M. M., 1992: Origin and tectonic implications of Pan-African amphibolites of Wadi Feiran, south Sinai. In Proceedings of the third conference on Geology of Sinai Development, Ismailia (Vol. 239, p. 248).

Evans, D.A., Mitchell, R.N., 2011. Assembly and breakup of the core of Paleoproterozoic-Mesoproterozoic supercontinent Nuna. Geology 39 (5), 443–446.

Eyal, M., Litvinovsky, B., Jahn, B.M., Zanvilevich, A., Katzir, Y., 2010. Origin and evolution of post-collisional magmatism: coeval Neoproterozoic calc-alkaline and alkaline suites of the Sinai Peninsula. Chem. Geol. 269 (3–4), 153–179.

Eyal, M., Be'eri-Shlevin, Y., Eyal, Y., Whitehouse, M.J., Litvinovsky, B., 2014. Three successive Proterozoic island arcs in the Northern Arabian-Nubian Shield: Evidence from SIMS U-Pb dating of zircon. Gondw. Res. 25 (1), 338–357.

Foster, M.D., 1960. Interpretation of the composition of trioctahedral mica. U.S. Geol Surv Prof Pap 354-B:11–49.

Fowler, A., Hassen, I.S., Osman, A.F., 2010. Neoproterozoic structural evolution of SE Sinai, Egypt: II. Convergent tectonic history of the continental arc Kid Group. J. Afr. Earth Sc. 58 (3), 526–546.

Fritz, H., Wallbrecher, E., Khudeir, A.A., El Ela, F.A., Dallmeyer, D.R., 1996. Formation of Neoproterozoic metamorphic complex during oblique convergence (Eastern Desert, Egypt). J. Afr. Earth Sc. 23 (3), 311–329.

Fritz, H., Dallmeyer, D.R., Wallbrecher, E., Loizenbauer, J., Hoinkes, G., Neumayr, P., Khudeir, A.A., 2002. Neoproterozoic tectonothermal evolution of the Central Eastern Desert, Egypt: a slow velocity tectonic process of core complex exhumation. J. Afr. Earth Sc. 34 (3–4), 137–155.

Fritz, H., Abdelsalam, M., Ali, K.A., Bingen, B., Collins, A.S., Fowler, A.R., Ghebreab, W., Hauzenberger, C.A., Johnson, P.R., Kusky, T.M., Macey, P., 2013. Orogen styles in the East African Orogen: a review of the Neoproterozoic to Cambrian tectonic evolution. J. Afr. Earth Sc. 86, 65–106.

Garrels, R.M., Mackenzie, F.T., 1971. Evolution of sedimentary rocks. Norton and Company:, New York, p. 394p.

Ghanem, H., Jarrar, G.H., McAleer, R.J., Passchier, C.W., Theye, T., Whitehouse, M.J., Wintsch, R.P., 2022. Drowned in granite-retrieving the tectono-metamorphic history of the Janub metamorphic complex, the northernmost part of the Arabian-Nubian Shield. Precambr. Res. 383, 106903.

Ghoneim, M.F., Noweir, M.A., Abu-Alam, T.S., 2015a. Magmatic evolution of the area around Wadi Kariem, Central Eastern Desert, Egypt. Arab. J. Geosci. 8 (11), 9221–9236.

Ghoneim, M.F., Heikal, M.T.S., El Dosuky, B.T., Abu-Alam, T.S., Sherif, M.I., 2015b. Neoproterozoic granites of Sharm El-Sheikh area, Egypt: mineralogical and thermobarometric variations. Arab. J. Geosci. 8 (1), 125–141.
Gray, D.R., Foster, D.A., Meert, J.G., Goscombe, B.D., Armstrong, R., Trouw, R.A.J., Passchier, C.W., 2008. A Damara orogen perspective on the assembly of southwestern Gondwana. Geol. Soc. Lond. Spec. Publ. 294 (1), 257–278.
Hamimi, Z., Arai, S., Fowler, A.R., El-Bialy, M.Z., 2021. The Geology of the Egyptian Nubian Shield. Springer International Publishing.
Hammarstrom, J.M., Zen, E.A., 1986. Aluminum in hornblende: an empirical igneous geobarometer. Am. Mineral. 71 (11–12), 1297–1313.
Hargrove, U.S., Stern, R.J., Kimura, J.I., Manton, W.I., Johnson, P.R., 2006. How juvenile is the Arabian-Nubian Shield? Evidence from Nd isotopes and pre-Neoproterozoic inherited zircon in the Bi'r Umq suture zone, Saudi Arabia. Earth Planet. Sci. Lett. 252 (3–4), 308–326.
Hassan, M., Abu-Alam, T.S., Stüwe, K., Fowler, A., Hassen, I., 2014. Metamorphic evolution of the Sa'al–Zaghra Complex in Sinai: Evidence for Mesoproterozoic Rodinia break-up? Precambr. Res. 241, 104–128.
Hassan, M., Abu-Alam, T. S., and Fowler, A. R., 2020. The Sinai Metamorphic Complexes from Rodinia Rifting to the Gondwana Collision. In the Geology of the Egyptian Nubian Shield, Springer, pp. 83-106.
Herron, M.M., 1988. Geochemical classification of terrigenous sands and shales from core or log data. J. Sediment. Res. 58 (5), 820–829.
Hey, M.H., 1954. A new review of the chlorites. Mineral. Mag. J. Mineral. Soc. 30 (224), 277–292.
Holdaway, M.J., Lee, S.M., 1977. Fe-Mg cordierite stability in high grade pelitic rocks based on experimental, theoretical, and natural observation. Contrib. Minerol. Petrol. 63, 175–198.
Holland, T., Blundy, J., 1994. Non-ideal interactions in calcic amphiboles and their bearing on amphibole plagioclase thermometry. Contrib. Miner. Petrol. 116, 433–447.
Hollister, L.S., Grissom, G.C., Peters, E.K., Stowell, H.H., Sisson, V.B., 1987. Confirmation of the empirical correlation of Al in hornblende with pressure of solidification of calc-alkaline plutons. Am. Mineral. 72 (3–4), 231–239.
Hoskin, P.W., Schaltegger, U., 2003. The composition of zircon and igneous and metamorphic petrogenesis. Rev. Mineral. Geochem. 53 (1), 27–62.
Jarrar, G., Stern, R.J., Saffarini, G., Al-Zubi, H., 2003. Late-and post-orogenic Neoproterozoic intrusions of Jordan: implications for crustal growth in the northernmost segment of the East African Orogen. Precambr. Res. 123 (2–4), 295–319.
Johnson, P.R., Kattan, F.H., Al-Saleh, A.M., 2004. Neoproterozoic ophiolites in the Arabian Shield: Field relations and structure. Develop. Precambr. Geol. 13, 129–162.
Johnson, P.R., Andresen, A., Collins, A.S., Fowler, A.R., Fritz, H., Ghebreab, W., Stern, R. J., 2011. Late Cryogenian-Ediacaran history of the Arabian-Nubian Shield: a review of depositional, plutonic, structural, and tectonic events in the closing stages of the northern East African Orogen. J. Afr. Earth Sc. 61 (3), 167–232.
Johnson, M.C., Rutherford, M.J., 1989. Experimental calibration of the aluminum-in-hornblende geobarometer with application to Long Valley caldera (California) volcanic rocks. Geology 17 (9), 837–841.
Johnson, P.R., Woldehaimanot, B., 2003. Development of the Arabian-Nubian Shield: perspectives on accretion and deformation in the northern East African Orogen and the assembly of Gondwana. Geol. Soc. Lond. Spec. Publ. 206 (1), 289–325.
Khudeir, A.A., Paquette, J.L., Nicholson, K., Johansson, Å., Rooney, T.O., Hamid, S., El-Rus, M.A.A., 2021. On the cratonization of the Arabian-Nubian Shield: Constraints from gneissic granitoids in south Eastern Desert, Egypt. Geosci. Front. 12 (4), 101148.
Kirkland, C.L., Smithies, R.H., Taylor, R.J.M., Evans, N., McDonald, B., 2015. Zircon Th/U ratios in magmatic environs. Lithos 212–215, 397–1341.
Kleemann, G.J., Twist, D., 1989. The compositionally-zoned sheet like granite pluton of the Bushveld Complex: Evidence bearing on the nature of A-type magmatism. J. Petrol. 30 (6), 1383–1414.
Kolodner, K., 2007. the Provenance of the Siliciclastic Section in Israel and Jordan: U-Pb Dating of Detrital Zircons. The Hebrew University of Jerusalem, Jerusalem 133.
Lachance, G., Traill, R., 1966. The theoretical influence coefficient method. Spectrosc 11, 43–48.
Leake, B.E., 1965. The relationship between composition of calciferous amphibole and grade of metamorphism. In: Pitcher, W.S., Flinn, G.W. (Eds.), Controls of Metamorphism. Wiley, NewYork, pp. 299–318.
Leake, B.E., 1978. Nomenclature of amphiboles. Am. Mineral. 63 (11–12), 1023–1052.
Leake, B.E., Woolley, A.R., Arps, C.E.S., Birch, W.D., Gilbert, M.C., Grice, J.D., 1997. Nomenclature of amphiboles: report of the subcommittee on amphiboles of the international mineralogical association, commission on new minerals and mineral names. Am. Mineral. 82, 1019–1037.
Li, Z.X., Bogdanova, S.V., Collins, A.S., Davidson, A., De Waele, B., Ernst, R.E., Fitzsimons, I.C.W., Fuck, R.A., Gladkochub, D.P., Jacobs, J., Karlstrom, K.E., Lu, S., Natapov, L.M., Pease, V., Pisarevsky, S.A., Thrane, K., Vernikovsky, V., 2008. Assembly, configuration, and break-up history of Rodinia: a synthesis. Precambr. Res. 160 (1–2), 179–210.
Li, Q.L., Li, X.H., Liu, Y., Tang, G.Q., Yang, J.H., Zhu, W.G., 2010. Precise U-Pb and Pb-Pb dating of Phanerozoic baddeleyite by SIMS with oxygen flooding technique. J. Anal. At. Spectrom. 25, 1107–1113.
Li, X.H., Liu, Y., Li, Q.L., Guo, C.H., Chamberlain, K.R., 2009. Precise determination of Phanerozoic zircon Pb/Pb age by multicollector SIMS without external standardization. Geochem. Geophys. Geosyst. 10 (4).
Liégeois, J.P., Stern, R.J., 2010. Sr–Nd isotopes and geochemistry of granite-gneiss complexes from the Meatiq and Hafafit domes, Eastern Desert, Egypt: no evidence for pre-Neoproterozoic crust. J. Afr. Earth Sc. 57 (1–2), 31–40.
Loizenbauer, J., Wallbrecher, E., Fritz, H., Neumayr, P., Khudeir, A.A., Kloetzli, U., 2001. Structural geology, single zircon ages and fluid inclusion studies of the Meatiq metamorphic core complex: Implications for Neoproterozoic tectonics in the Eastern Desert of Egypt. Precambr. Res. 110, 357–383.
Ludwig, K.C., 2007. In: User's manual for Isoplot 3.7. Berkley Geochronology Center, Berkley, p. 70.
Lutgens, F., Tarbuck, E.J., Tasa, D., 2018. Essentials of geology, 13th ed. Pearson, Hoboken, New Jersey, USA.
Maniar, D.D., Piccolo, P.M., 1989. Tectonic Discrimination of granitoids. Geol. Soc. Am. Bull. 101, 635–643.
Meert, J.G., Torsvik, T.H., 2003. The making and unmaking of a supercontinent: Rodinia revisited. Tectonophysics 375 (1–4), 261–288.
Meyer, S.E., Passchier, C., Abu-Alam, T., Stüwe, K., 2014. A strike-slip core complex from the Najd fault system. Arabian shield. Terra Nova 26 (5), 387–394.
Middleton, M.F., 1989. A model for the formation of intracratonic sag basins. Geophys. J. Int. 99 (3), 665–676.
Miller, C.F., Stoddard, E.F., Bradfish, L.J., Dollase, W.A., 1981. Composition of plutonic muscovite: Genetic implications. Can. Mineral. 19, 25–34.
Miyashiro, A., 1975. Volcanic rock series and tectonic setting. Annu. Rev. Earth Planet. Sci. 3 (1), 251–269.
Moghazi, A.K.M., 2003. Geochemistry of a Tertiary continental basalt suite, Red Sea coastal plain, Egypt: petrogenesis and characteristics of the mantle source region. Geol. Mag. 140 (1), 11–24.
Moghazi, A.M., Ali, K.A., Wilde, S.A., Zhou, Q., Andersen, T., Andresen, A., Abu El- Enen, M.M., Stern, R.J., 2012. Geochemistry, geochronology, and Sr–Nd isotopes of the Late Neoproterozoic Wadi Kid volcano-sedimentary rocks, Southern Sinai, Egypt: implications for tectonic setting and crustal evolution. Lithos 154, 147–165.
Morimoto, N., 1988. Nomenclature of pyroxenes. Mineral. Petrol. 39 (1), 55–76.
Nance, R.D., Murphy, J.B., Santosh, M., 2014. The supercontinent cycle: a retrospective essay. Gondw. Res. 25 (1), 4–29.
O'Connor, J.T., 1965. A classification for quartz-rich igneous rocks based on feldspar ratios. US Geol. Survey Professional Paper B 525, 79–84.
Patchett, P.J., Chase, C.G., 2002. Role of transform continental margins in major crustal growth episodes. Geology 30 (1), 39–42.
Pearce, J.A., Cann, J.R., 1973. Tectonic setting of basic volcanic rocks determined using trace element analyses. Earth Planet. Sci. Lett. 19, 290–300.
Pearce, J.A., Harris, N.B., Tindle, A.G., 1984. Trace element discrimination diagrams for the tectonic interpretation of granitic rocks. J. Petrol. 25 (4), 956–983.
Perchuk, L. L., Lavrent'Eva, I. V., 1983. Experimental investigation of exchange equilibria in the system cordierite-garnet-biotite. In: Kinetics and equilibrium in mineral reactions. Springer, New York, NY,3, 199-239.
Perchuk, L.L., Aranovich, L.Y., Podlesskii, K.K., Lavrant'eva, I., Gerasimov, V.Y., Fed'Kin, V.V., Berdnikov, N.V., 1985. Precambrian granulites of the Aldan shield, eastern Siberia. USSR. J. Metamorphic Geol. 3 (3), 265–310.
Plyusnina, L.P., 1982. Geothermometry and geobarometry of plagioclase –hornblende bearing assemblages. Contrib. Miner. Petrol. 45, 140–146.
Reymer, A.P.S., Oertel, G., 1985. Horizontal cleavage in southeastern Sinai: the case for a coaxial strain history. J Struct Geol 7, 623–636.
Richard, L.R., 1995. MinPet: Mineralogical and Petrological Data Processing System, Version 2.02. MinPet Geological Software, Québec.
Robinson, F.A., Foden, J.D., Collins, A.S., Payne, J.L., 2014. Arabian Shield magmatic cycles and their relationship with Gondwana assembly: insights from zircon U-Pb and Hf isotopes. Earth Planet. Sci. Lett. 408, 207–225.
Rogers, J.J., Santosh, M., 2002. Configuration of Columbia, a Mesoproterozoic supercontinent. Gondw. Res. 5 (1), 5–22.
Roser, B.P., Korsch, R.J., 1986. Determination of tectonic setting of sandstone-mudstone suites using SiO_2 content and K_2O/Na_2O ratio. J. Geol. 94 (5), 635–650.
Schmidt, M.W., 1992. Amphibole composition in tonalite as a function of pressure: an experimental calibration of the Al-in-hornblende barometer. Contrib. Miner. Petrol. 110 (2), 304–310.
Shimron, A.E., 1985. Evolution of the Kid Group, southeast Sinai Peninsula: thrusts, mélanges, and implications for accretionary tectonics during the late Proterozoic of the Arabian-Nubian Shield—reply to comments. Geology 13, 156–157.
Stacey, J.T., Kramers, 1., 1975. Approximation of terrestrial lead isotope evolution by a two-stage model. Earth and planetary science letters 26 (2), 207–221.
Stern, R.J., 1994. Arc assembly and continental collision in the Neoproterozoic East African Orogen: implications for the consolidation of Gondwanaland. Annu. Rev. Earth Planet. Sci. 22 (1), 319–351.
Stern, R.J., 2008. Modern-style plate tectonics began in Neoproterozoic time: An alternative interpretation of Earth's tectonic history. When did plate tectonics begin on planet Earth 265, 280.
Stern, R.J., Johnson, P., 2010. Continental lithosphere of the Arabian Plate: a geologic, petrologic, and geophysical synthesis. Earth Sci. Rev. 101 (1–2), 29–67.
Stern, R.J., Johnson, P.R., Kröner, A., Yibas, B., 2004. Neoproterozoic ophiolites of the Arabian-Nubian shield. Develop. Precambr. Geol. 13, 95–128.
Stern, R.J., Manton, W.I., 1987. Age of Feiran basement rocks, Sinai—implications for late Precambrian crustal evolution in the northern Arabian-Nubian Shield. J. Geol. Soc. Lond. 144, 569–575.
Stoeser, D.B., Camp, V.E., 1985. Pan-African microplate accretion of the Arabian Shield. Geol. Soc. Am. Bull. 96 (7), 817–826.
Streckeisen, A., 1976. To each plutonic rocks its proper name. Earth Sci. Rev. 12, 1–33.
Thompson, A.B., 1976. Mineral reactions in pelitic rocks. I. Prediction of PTX (Fe-Mg) phase relations.
Wells, P.R.A., 1979. PT conditions in the Moines of the Central Highlands, Scotland. J. Geol. Soc. 136 (6), 663–671.

Wiedenbeck, M., Hanchar, J.M., Peck, W.H., Sylvester, P., Valley, J., Whitehouse, M., Kronz, A., Morishita, Y., Nasdala, L., Fiebig, J., Franchi, I., Girard, J.P., Greenwood, R.C., Hinton, R., Kita, N., Mason, P.R.D., Norman, M., Ogasawara, M., Piccoli, R., Rhede, D., Satoh, H., Schulz-Dobrick, B., Skar, O., Spicuzza, M.J., Terada, K., Tindle, A., Togashi, S., Vennemann, T., Xie, Q., Zheng, Y.F., 2004. characterisation of the 91500-zircon crystal. Geostand. Geoanal. Res. 28 (1), 9–39.

Wilson, R.W., Houseman, G.A., Buiter, S.J.H., McCaffrey, K.J., Doré, A.G., 2019. Fifty years of the Wilson Cycle concept in plate tectonics: an overview. Geol. Soc. Lond. Spec. Publ. 470 (1), 1–17.

Wright, J.B., 1969. A simple alkalinity ratio and its application to questions of non-orogenic granite genesis. Geol. Mag. 106 (4), 370–384.

Wu, C.M., Chen, H.X., 2015. Revised Ti-in-biotite geothermometer for ilmenite-or rutile-bearing crustal metapelites. Sci. Bull. 60 (1), 116–121.

Yeshanew, F. G., 2017. Crustal evolution of the Arabian–Nubian Shield: insights from zircon geochronology and Nd–Hf–O isotopes (Doctoral dissertation, Department of Geological Sciences, Stockholm University).

Zhao, G., Cawood, P.A., Wilde, S.A., Sun, M., 2002. Review of global 2.1–1.8 Ga orogens: implications for a pre-Rodinia supercontinent. Earth Sci. Rev. 59 (1–4), 125–162.

Zoheir, B., Abd El-Rahman, Y., Kusky, T., Xiong, F., 2021. New SIMS zircon U-Pb ages and oxygen isotope data for ophiolite nappes in the Eastern Desert of Egypt: Implications for Gondwana assembly. Gondw. Res. 105, 450–467.